School of Chemistry

Thermal hydrogen loading of single and polycrystalline boron doped diamonds

Axel Persson

This thesis is submitted in partial fulfilment of the requirements for the Honours Degree of BSc at the University of Bristol

[Supervisor: Neil Fox]

[Second Assessor: Paul May]

[Physical and Theoretical Chemistry]

Abstract

Diamonds have proven to be a wide band gap semiconductor with outstanding electronic properties, surpassing those of its silicon carbide and gallium nitride. Due to this, diamond is deemed as one of the most optimum semiconductors used in the direct conversion of beta decay energy into electricity. By utilising semiconductors such as a diamond, these betavoltaic devices offer low-power, ultra-long-life batteries suitable for application in hard-to-reach places.

While prototype batteries using diamond with other beta sources have been demonstrated, there is little literature on tritium-based diamond betavoltaic devices. This study aims to investigate a possible route towards immobilising tritium within the diamond semiconductors, offering the benefit of placing the beta source within the semiconductor converter. However, due to the difficulties surrounding obtaining and using tritium, deuterium was used as a suitable analogue.

In this study, deuterium was thermally loaded into diamonds by exposing samples to a 1000 °C deuterium atmosphere (~350 torr) using a Nabertherm compact tube furnace. The samples loaded with deuterium involved pristine, graphitised, and boron-doped single crystal diamonds (SCDs), along with freestanding boron-doped polycrystalline diamonds (BDPCD). The samples were obtained from Element Six, with the boron-doped layers on the single crystal diamonds being grown in-house using microwave plasma chemical vapour deposition. Additionally, two further samples, one intrinsic and one boron doped, with Frenkel defects induced 5 µm under the surface, were investigated. The defects were induced *via* laser at the Department of Engineering at the University of Oxford.

After deuterium loading, samples were analysed using secondary ion mass spectrometry (SIMS), with one boron-doped SCD sample being analysed using thermal desorption spectroscopy (TDS). The TDS results demonstrate that the thermal loading of deuterium was successful, with the atoms seemingly incorporating into stable binding sites within the diamond lattice. Through calibration of the instrument, deuterium content was determined to be 1.4 x 10^{16} atoms/cm^2. The SIMS results indicate that deuterium is also present much deeper in the diamond, with deuterium counts being observed at depths up to 7 µm. However, due to the uncertainty of the SIMS instrument, clear conclusions on implantation depth cannot be drawn. Additionally, samples which had a higher number of defects (BDPCD, graphitised SCD) are shown to retain higher amounts of deuterium than relatively defect-free samples (pristine SCD, BDSCD). From the SIMS results, it was difficult to determine whether the induced Frenkel defects had any effect on the deuterium retention of the samples, requiring further testing and analysis to obtain any clear conclusions.

The TDS results illustrate that the thermal loading of deuterium into diamond is effective, opening possibilities for tritium-loaded diamond betavoltaics. Furthermore, qualitative SIMS analysis suggests that polycrystalline diamond would be the most suitable for this application, offering the highest deuterium retention at a lower cost.

Acknowledgements

First of all, I would like to express my gratitude to Professor Neil Fox for all his help and guidance. The thoughtful discussions with him have not only helped my project but have also fueled my interest in the subject. Also, the weekly project meetings have provided me with much insight and have been crucial towards putting me in the right direction and completing my project.

I would also like to thank Professor Paul May for his insightful advice and second opinion on matters. The meetings I had with him offered me valuable advice and allowed me to see things from a scientific perspective. I would also like to thank him for organising the BUDGie meals, which have been a highlight of this year.

I would also like to thank Dr. Ramiz Zulkharnay for all his help by answering all the questions that I had and for offering his vast experience and insight towards the problems I faced.

For teaching me how to operate the reactor, LEXT, the laser cutter, and for always being a friendly face to chat with, I would like to thank Catherine Monk. For numerous helpful discussions regarding my TDS or SIMS data, I would like to thank both James Pittard and Liam Cullingford, and I wish them the best with their postdoctoral journeys. I would also like to extend my thanks to Dr. James Smith, whose help was crucial in operating the tube furnace and not blowing the lab up. I would also like to thank the rest of the BUDGie group, who made my time in the lab a lot more enjoyable.

Lastly, I would like to thank my fellow diamond boys: Ben, Jacob, and James, who helped and supported me through many late-night and weekend writing sessions. I wish them well in their future endeavours, and I hope they remember to ‘Live Más.’

Table of Contents

i. List of Figures

ii. List of Tables

iii. List of Abbreviations

HPHT	High Pressure High Temperature
CVD	Chemical Vapour Deposition
HFCVD	Hot Filament Chemical Vapour Deposition
MWCVD	MicroWave Chemical Vapour Deposition
FOM	Figures Of Merit
BDD	Boron Doped Diamond
SBD	Schottky Barrier Diode
DSD	Diamond Schottky Diode
ODD	Ookuma Diamond Device
DFT	Density Functional Theory
PCD	PolyCrystalline Diamond
LWR	Light Water Reactor
HWR	Heavy Water Reactor
TRF	Tritium Removal Facility
SCD	Single Crystal Diamond
TDS	Thermal Desorption Spectroscopy
BDPCD	Boron Doped PolyCrystalline Diamond
BDSCD	Boron Doped Single Crystal Diamond
SIMS	Secondary Ion Mass Spectrometry
SCCM	Standard Cubic Centimetres per Minutes
MFC	Mass Flow Controller
t-PA	trans-PolyAcetylene
TOF	Time Of Flight
UHV	Ultra-High Vacuum

1. Introduction

The electronics and battery industry lie at the heart of the decarbonisation and green energy transitions in the modern world. With the vast developments and cost-cutting of photovoltaic cells combined with the worsening public image of nuclear reactors, the idea of harnessing energy from radioactivity has fallen behind. Diamond, a highly regarded material, could revitalise and innovate the radioactive energy industry through its remarkable properties.[1]

Although consisting of solely carbon and being arguably indistinguishable from many other gemstones, diamonds have fascinated humans throughout history. Being one of the hardest materials, diamond also exhibits high thermal conductivity, excellent chemical stability, and radiation hardness, all due to its distinctive molecular configuration.[2] In diamond, sp^3 hybridised carbons are arranged in a covalent tetrahedral lattice (Figure 1), giving rise to the remarkable hardness of diamonds, which ranks 10 on the Mohs scale.

Graphite, another allotrope of carbon, comprises layers of hexagonally bonded sp^2 carbons (Figure 1) with one valency delocalised perpendicular to the plane. The delocalised electrons make graphite an excellent electrical conductor, being a crucial component in lithium-ion batteries, the fastest growing batteries in the market.[3] Similarly to graphite, diamond could become a crucial component in betavoltaic cells, a form of radioisotope generator that produces electricity from beta decay. To achieve this, the diamonds used require very specific impurities, of which almost none occur naturally.[4]

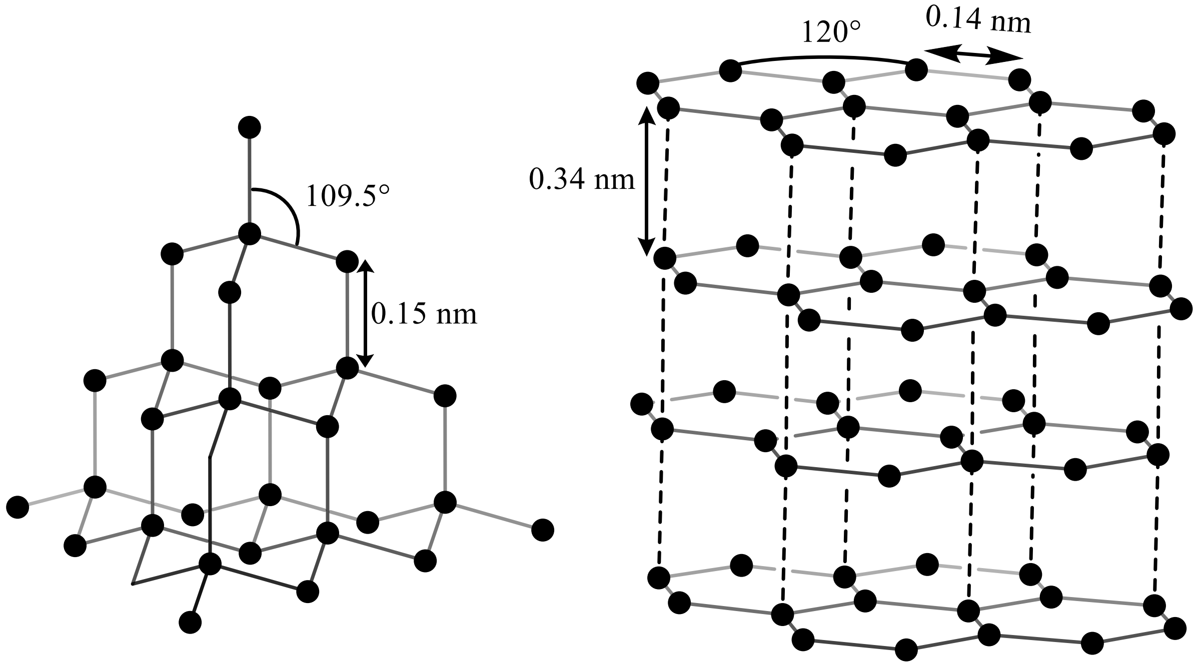

Figure 1. The different bonding structures of diamond (left) and graphite (right). The tetrahedral lattice, along with strong covalent bonds, results in diamond being the hardest naturally occurring material. Graphite consists of layers of hexagonally bonded carbon (Graphene) held together by van der Waal forces between delocalised electrons. Unlike graphite, intrinsic diamond does not possess any free electrons and thus does not conduct electricity in its intrinsic state.

1.1 The theory of growing diamonds

Surprisingly, diamond is not the most stable allotrope of carbon, with graphite being more stable at standard conditions.[5] Diamonds are metastable, meaning that there is a large energy barrier preventing the spontaneous conversion to graphite. A consequence of this is the difficulty of turning other carbon forms into diamond, as graphite is the thermodynamically stable form. One approach to grow diamonds was to replicate the natural process. High Pressure High Temperature (HPHT) growth involves a carbon source with a metal catalyst being compressed to tens of thousands of atmospheres at temperatures reaching up to 2000 K.[6] While HPHT can effectively produce large diamonds, the metal catalyst and other impurities usually incorporate into the diamond, resulting in yellow coloration and inferior electronic properties.[4, 7]

As the standard enthalpies of diamond and graphite are only separated by a negligible difference (~2 kJ mol^{-1}), a carbon vapour, which has an enthalpy difference of ~700 kJ mol^{-1}, would theoretically condense into diamond and graphite with almost equal probability.[8, 9] This technique was further improved upon by the addition of excess hydrogen to the vapour, limiting graphite nucleation and allowing for only diamond to condense.[10] The new technique, deemed Chemical Vapour Deposition (CVD), allowed for thin diamond films to grow at much faster rates than HPHT by using activated gas mixtures.

The CVD growth process is simplified in Figure 2, where a stepwise interaction involving a carbon containing radical (common consensus being the methyl radical) and a reactive site on the substrate surface leads to a growing diamond lattice. CVD diamond growth is often referred to as ‘five steps forwards, but four steps back’ as hydrogen atoms often interfere with the steps in the growing process, hindering progress.[11]

Additionally, the aforementioned model is also an oversimplification, with Ashfold and May predicting 20 major steps involved solely in the formation of the methyl radical.[12] The complexity of the process led to Bachmann *et al.* collecting data from over 70 growth experiments and producing a triangle showing suitable diamond growing conditions (Figure 3).[13] Through further computational modelling, Petherbridge and May have determined that the boundaries between diamond growth correspond to changes in the methyl radical concentration and a $[H]/[C_2H_2]$ ratio, reiterating the importance of the methyl and hydrogen species in diamond growth.[14] Due to hydrogen being a crucial part of the process, modern CVD techniques involve gas mixtures consisting of mostly (~99%) H_2, leading to hydrogen being the most abundant impurity within CVD grown diamonds.[15]

Within CVD syntheses, there are numerous ways of gas excitation, with the two main groups being heated gas and ionisation plasma methods. Thermally induced CVD growth includes hot filament CVD (HFCVD), which activates the gas phase using a hot metal filament. Molecules which approach the filament thermally dissociate and diffuse onto the surface of the substrate, producing diamond crystals.[16, 17] HFCVD is a technique that allows for uniform diamond deposition over large areas, however, it lacks control over film morphology and gives rise to unwanted impurities from the degradation of the metal filament.

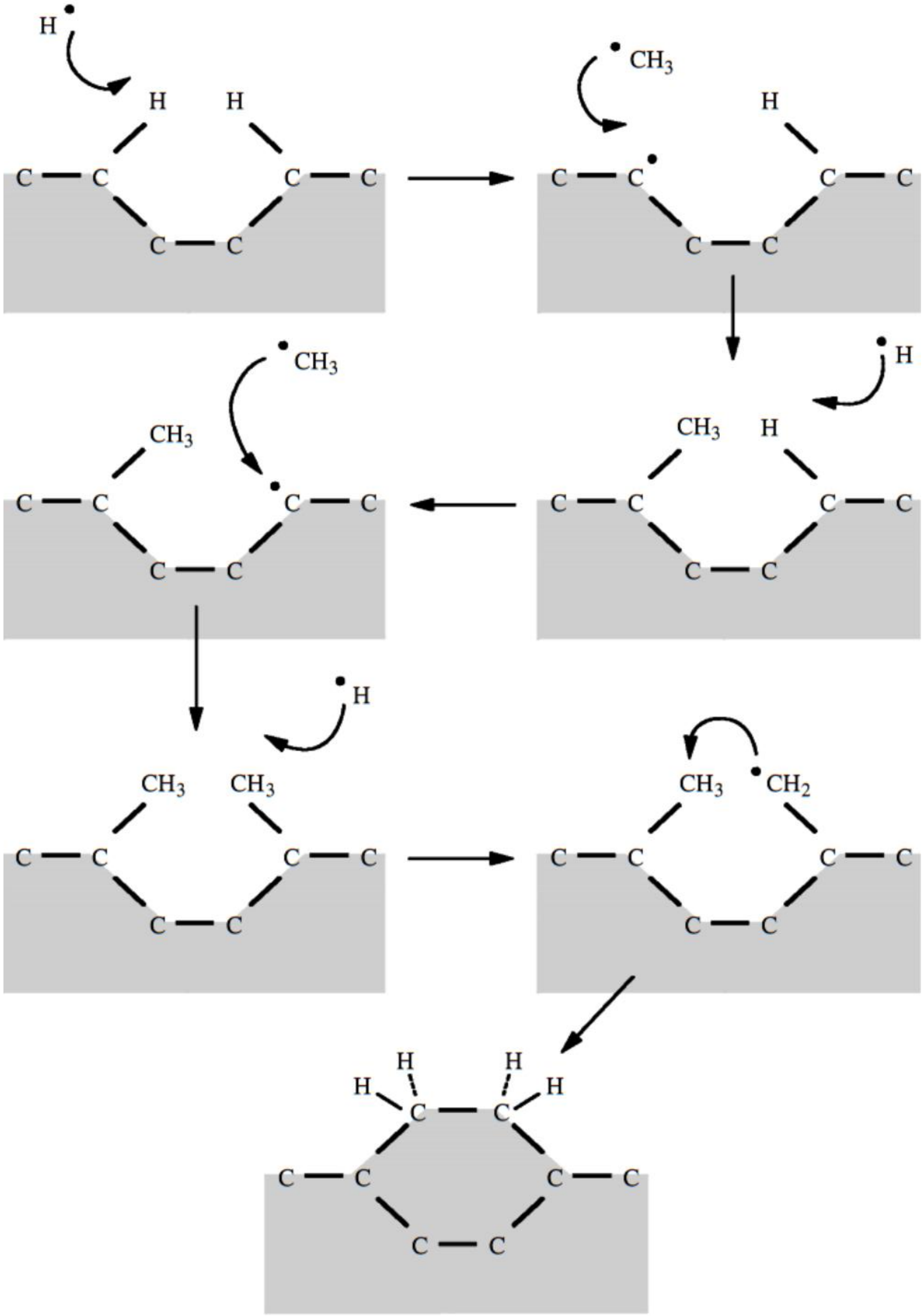

Figure 2. Simplified mechanism for the growth of diamonds using chemical vapour deposition. The schematic demonstrates the stepwise addition of methyl radical to generate the diamond lattice. Note that each step is also reversible, slowing down the growing process. Figure taken from Ref. 11

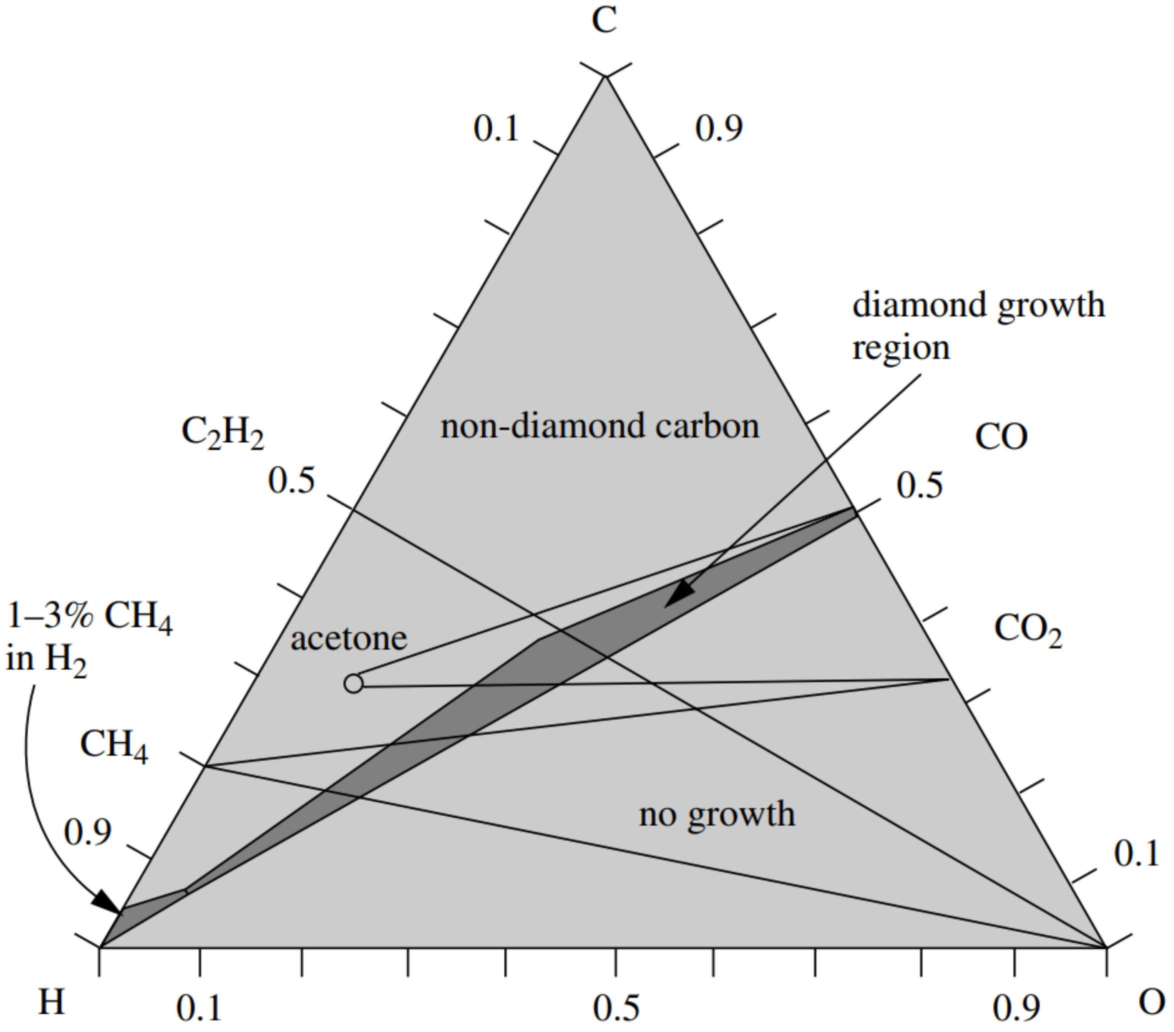

Figure 3. The Bachmann triangle C-H-O composition diagram. The shaded region shows conditions at which diamonds grow. Above the region, non-diamond carbon is formed, while no growth is observed under the region. Most CVD growths are performed within the small region in the lower left-hand corner. Figure taken from Ref. 11

On the other hand, the gas can be activated *via* ionisation plasma methods, such as with microwave plasma CVD (MWCVD). MWCVD is the most common form of CVD used in laboratories due to its ability to produce films with much lower levels of undesirable impurities.[18] MWCVD utilises microwaves (2.54 GHz) generated by a magnetron to activate the gas mixtures. The chambers used within MWCVD reactors are specifically designed to act as a resonant cavity to maximise energy transfer and allow for easier plasma ignition (Figure 4). This phenomenon limits the chamber size, as it needs to be inversely proportional to the frequency of the microwave, resulting in a maximum plasma dimension of 6 cm at 2.54 GHz. To produce larger diamond films, a lower frequency microwave of 915 MHz is used along with a larger chamber, increasing the plasma size to 16 cm.[19] While it restricts the size of the diamond film grown, MWCVD's ability to control impurities and produce high quality diamonds makes its one of the most promising techniques for electronic applications.[20]

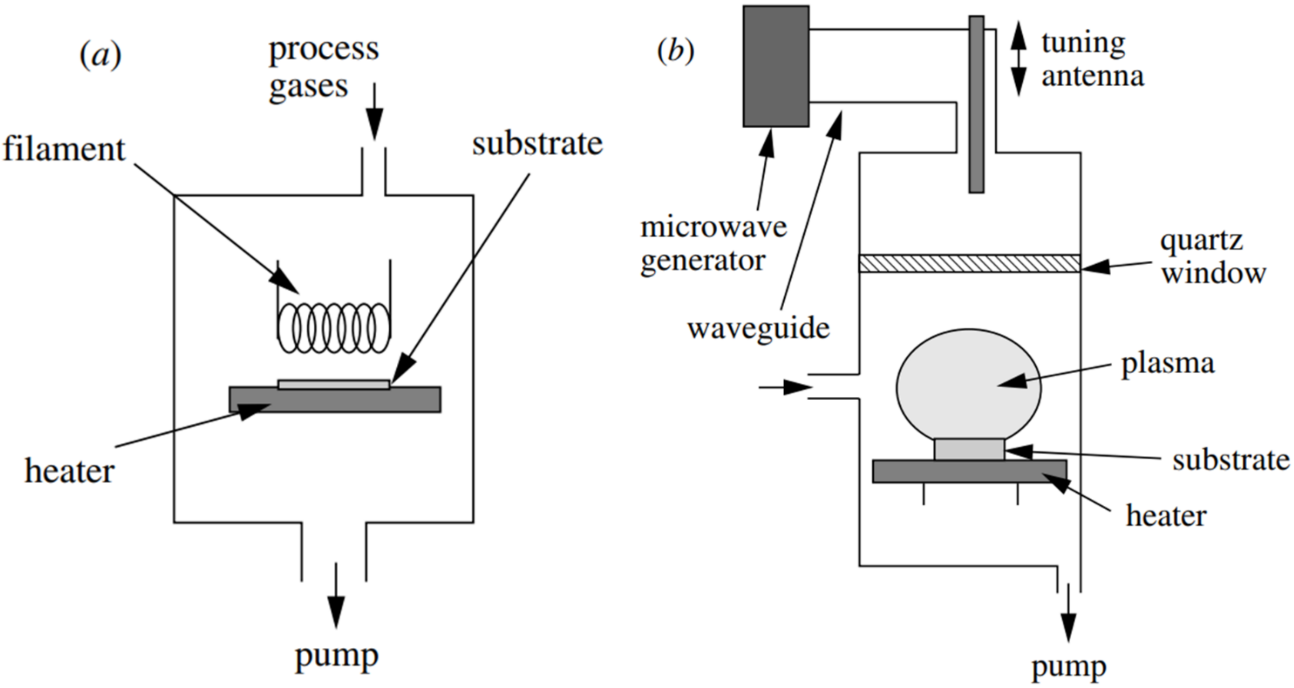

Figure 4. Schematics of a) HFCVD and b) ASTEX MWCVD commonly used to grow diamonds. Figure taken from Ref. 11

1.2 Diamond as an electronic material

Diamond is a wide-gap material with an indirect band gap of 5.48 eV.[21] Depending on impurity concentrations, diamond can demonstrate excellent semiconducting properties (Table 1), surpassing other common wide-gap semiconductors like gallium nitride (GaN) and silicon carbide (SiC).[22] The same can be said for figures of merit (FOM), which are good indicators of the utility of various materials within specific use cases.

Johnson's FOM describes the suitability of a material for high power and frequency uses, such as in transistors.[23] Similarly, Keyes' FOM is another key figure which describes the thermal limit of high-frequency switching in semiconductor materials, a useful comparison for devices which operate at high temperatures.[24] Meanwhile, Baliga's FOM defines the parameters for reducing conduction losses, being a good measure of material performance in low-frequency unipolar devices.[25] Within these FOM, CVD diamond again surpasses its competitors, highlighting its superiority as an electron material and its ability to slot into various applications.

Table 1. Material Properties of CVD-grown diamond compared to common semiconductors Si, 4H-SiC, and GaN. 4H-SiC was chosen for the comparison as it is deemed the most suitable for electronic applications. Table modified from Ref. 22

Property at 273 K	Silicon	4H-SiC	GaN	CVD Diamond	Application Benefits
Band Gap (eV)	1.1	3.2	3.44	5.47	High Temperature
Breakdown Field (MV cm^{-1})	0.3	3	5	10	High Voltage
Thermal Conductivity (W k^{-1} cm^{-1})	1.5	5	1.3	24	High Power
Electron Mobility (cm^2 V^{-1} s^{-1})	1450	900	440	4500	Performance Speed
Hole Mobility (cm^2 V^{-1} s^{-1})	480	120	200	3800	Performance Speed
Johnson's FOM	1	410	280	8200	High power & frequency
Baliga's FOM	1	290	910	17200	Unipolar device performance
Keyes' FOM	1	5.1	1.8	32	Thermal limit of frequency switching

However, to take advantage of these electronic properties and apply them towards electronic devices, diamond must be doped with impurities. Doping is a common process where an intrinsic material has a small number of foreign atoms introduced to add electrons or holes. When comparing the band gap of an n (negative) and p (positive) type semiconductor against an intrinsic, the effects of doping become clear (Figure 5). The introduction of a lower level accepting band reduces the energy needed to promote an electron from the valence band, generating more positive holes, hence being called p-type doping. Meanwhile, the introduction of a higher-level donating band reduces the band gap, increasing the number of negatively charged electrons in the conduction band and thus is called n-type doping.

For diamond, trivalent and pentavalent atoms would be suitable dopants to generate p-type and n-type semiconductors, respectively. One such example is boron, with boron doping into diamond being able to convert the usually insulating material to an effective p-type semiconductor.[26] As boron doping has a relatively low activation energy (0.37 eV), a high level of doping is possible to the point where boron doped diamond (BDD) can exhibit near-metallic conductivity.[27, 28] The actual process of growing p-doped diamond *via* MCVD is simple, as only a tiny fraction of boron-containing molecules are needed in the gas mixture. On the other hand, finding a suitable candidate and process for n-type doping of diamond has remained one of the most difficult tasks, being deemed the 'Holy Grail' of diamond research.[29] This difficulty is largely due to the tight diamond lattice restricting the size of the dopants, limiting the choices of dopants to light atoms.[30] While n-type doping of diamond using phosphorous or nitrogen is achievable, the two atoms generate deep donor levels, hindering its utility in electronics.[31] A consequence of the elusive n-type dopant has led to diamond electronics research focusing mostly on unipolar devices, which only need one doped semiconductor.[22]

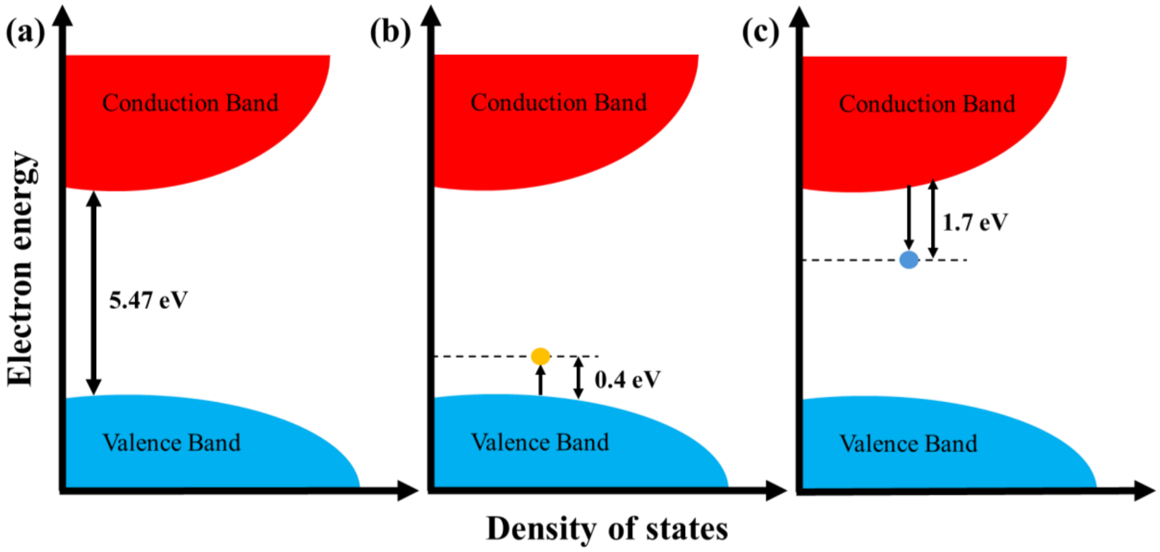

Figure 5. Band gap diagrams of an (a) Intrinsic, (b) Boron-doped, and (c) Nitrogen-doped diamond. The introduction of boron into the diamond creates a shallow acceptor level at 0.4 eV. Meanwhile, the introduction of nitrogen results in a deep donor level at roughly 1.7 eV. Due to the depth of the donor level, nitrogen doped diamonds have their electronic properties hindered by larger energy barriers.

1.3 Schottky Diodes

Schottky barrier diodes (SBD) are an example of such unipolar devices, as they only require one type of semiconductor. When compared to conventional diodes, SBDs consist of a junction between a semiconductor and a metal (a Schottky barrier) rather than a semiconductor-semiconductor junction (Figure 6). SBDs offer unique advantages with higher sensitivities and faster recovery times compared to PN or PIN junction diodes.[32] In principle, SBDs act like normal diodes, where an applied voltage allows for current to flow easily in one direction while offering high resistance in the other, acting as a one-way switch. The one-way characteristics result from the formation of a potential barrier between the semiconductor and the metal, which shifts depending on the voltage applied (also referred to as a bias). SBDs have a lower forward voltage drop, the voltage required for a forward current to pass, leading to a higher efficiency with less energy lost to heat.[33] Conversely, they suffer from low breakdown voltages, typically being lower than 50 V. A consequence of this is reverse leakage currents being higher than in conventional PN junctions. Despite that, implementation of Schottky diodes as a bypass in solar cells has demonstrated enchantment in photo-response and efficiency due to their lower forward drop voltages.[33, 34]

Research into diamond Schottky diodes started only in the late 1980s, with one of the earliest CVD diamond Schottky diodes (DSD) already reporting a room temperature breakdown voltage of 200 V.[35] Since then, DSD have yielded innovations within the field, with BDD

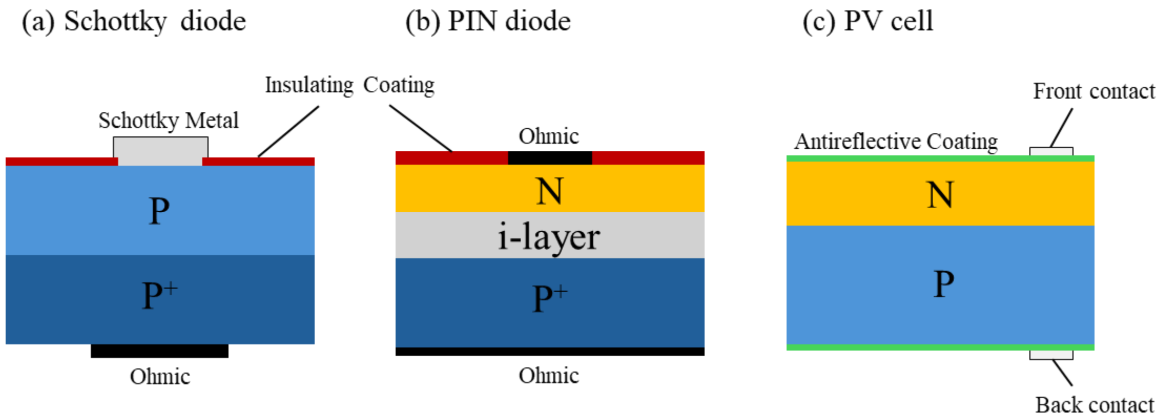

Figure 6. Comparisons of common semiconductor devices. (a) A vertical Schottky barrier diode using only P-type semiconductors with P^+ signifying a layer with higher doping concentration. A Schottky contact is used to form a Schottky junction between the semiconductor and metal. (b) A PIN diode consisting of an intrinsic semiconductor sandwiched between a P^+ and a N layer, with Ohmic contacts on both the front and the back of the diode. (c) A simple photovoltaic (PV) cell using a PN junction. Due to their indirect band gap, diamond semiconductors cannot be utilised for PV applications, which require direct band gaps. Diagrams modified from Ref. 42

incorporated as a key component in the first Schottky diode to operate at 1000 °C.[36] In 2015, a DSD which reported breakdown voltages of 713 V at 400 °C was produced, already being at the cusp of the theoretical limits of SiC at high temperatures.[37] The replacement of SiC diodes with DSD in high-temperature applications is expected to reduce energy loss by 90%, conveying diamonds' pivotal influence.[38] There have also been tremendous improvements from the 200-volt breakdown value, with a DSD developed in 2003 recording the highest breakdown value (>6 kV) of any semiconductor Schottky diode.[39] This record value is a result of MWCVD's remarkable selectivity over impurities combined with further annealing to remove embedded hydrogen, producing an exceptionally pure semiconducting diamond.

Even with these promising results, diamond Schottky diodes have yet to enter the market, with only prototypes being brought forth. In order for diamond power devices to take hold, many challenges related to material production, reliability, device fabrication, and integration will have to be tackled.[40] This sentiment is echoed in the diamond semiconductor market, which experts expect to grow only by $200,000 from 2022 to 2028, falling behind other semiconductor substrates.[41] However, various investors and startups still seem to believe that there is much promise behind diamond semiconductors, with startups garnering much attention and funding in recent years. Ookuma Diamond Device (ODD), a startup in Japan, has raised ~$27 million in 2024 to produce the world's first diamond semiconductor manufacturing plant.[42] Diamfab, another startup specialising in diamond semiconductors, have secured annual funding of $9.2 million in 2024 from various investors.[43] Thus, it is clear that the diamond semiconductor market is still emerging, with various innovations still being discovered and researched upon. The most eye-catching of which is the announcement by the University of Bristol in 2016 describing a diamond battery made from nuclear waste.[44]

2. Betavoltaic cells

Akin to how SBDs are utilised in solar cells, the diodes can be applied to nuclear batteries, acting as direct converters of nuclear energy into electricity (Figure 7). Radioisotope batteries, initially theorised in 1913, utilise the high energy density found within decaying radioisotopes to create extremely long-lasting batteries.[45] Radioisotope decay results from unstable nuclei that have too many or too few neutrons, which undergo the process to return to stable nuclear configurations. The decay itself is a random process, being impossible to predict at an atomic level and only approximated for the bulk. There are three main processes of radioactive decay: alpha, beta, and gamma. In alpha decay, an unstable parent nucleus forms a daughter nucleus by the release of an alpha particle (helium 4 nucleus) consisting of two protons and two neutrons.[46] The resulting daughter nucleus is often in an excited state where it decays further *via* the emission of gamma photons (gamma decay). On the other hand, in beta decay, a neutron decays into a proton, releasing an electron and an anti-neutrino. Similar to alpha decay, beta decay can also lead to an excited nucleus, giving rise to further gamma decay.

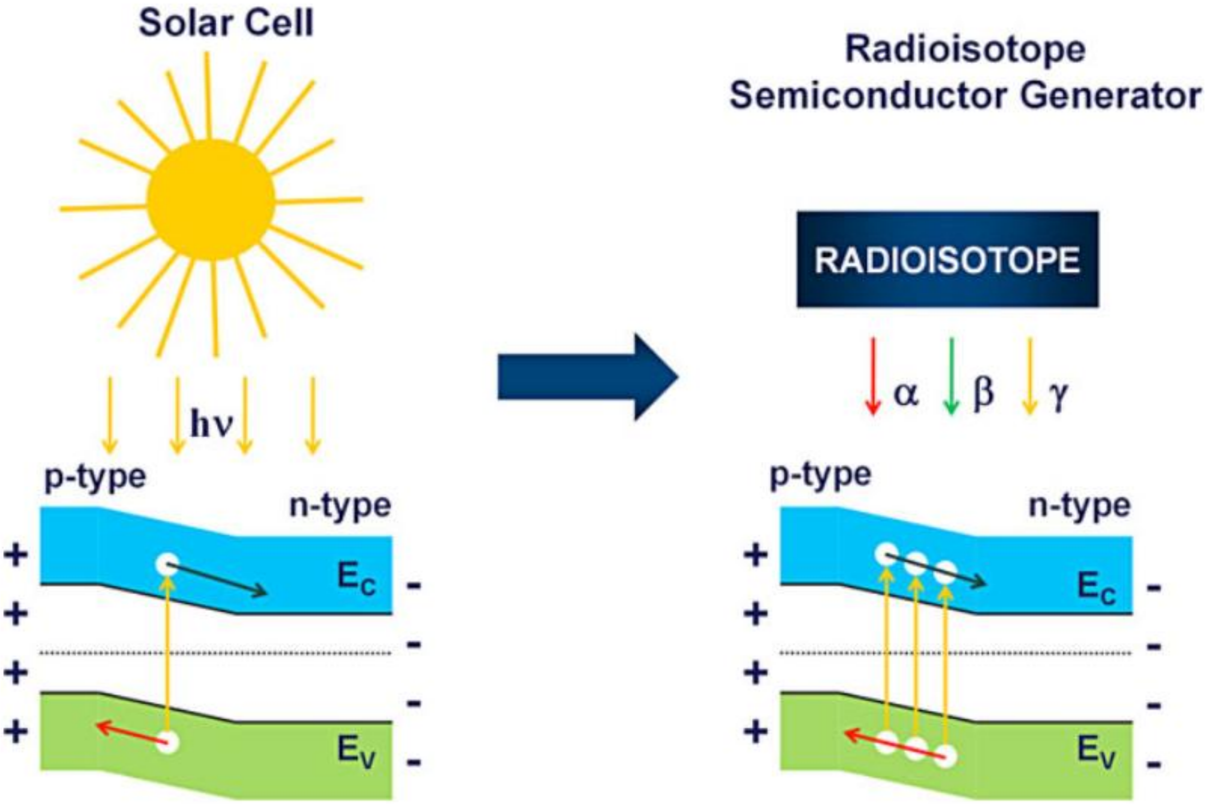

Figure 7. Comparison of the familiar solar cell and the principle of operation for a solid-state radioisotope generator using semiconductor materials as direct energy converters. Figure modified from Ref. 1

To harness the energy of radioisotopes, high-energy particles emitted from the decay process promote electrons, generating electron-hole pairs (Figure 7). The pairs which are generated within the depletion region are pulled through the junction by the depletion field, producing electric power. Batteries which tap into alpha and beta decay are deemed alphavoltaics and betavoltaics, respectively. Gammavoltaic cells have also been produced but are challenged by the high penetrating nature of gamma rays, requiring various protective measures.[47] Likewise, alphavoltaics suffer from severe degradation of the semiconductor crystal by the high-energy alpha particles, leading to lower efficiency and loss of performance over time.[48] These disadvantages have led to betavoltaics becoming the most attractive choice for radioisotope batteries, being applicable as very small, reliable, and durable power sources.[49]

The development of betavoltaic cells follows closely to the history of Schottky diodes. The theoretical maximum efficiency of betavoltaics has been in debate, with the value also depending on both the semiconductor material and the metal contact. Olsen theorised that the use of wide band gap semiconductor junctions in betavoltaics reduced current leakage, with higher efficiency also correlating with larger band gaps.[50, 51] Similar to the Shockley Queisser limit frequently discussed in the field of photovoltaics, betavoltaics are supposedly limited to a maximum conversion efficiency proportional to the band gap. In 1968, Klein proposed a phenomenological model to understand radiation ionisation energies in semiconductors. Through various calculations, the model demonstrates that the average radioactive energy consumed by each electron-hole pair is directly dependent on the band gap and optical photon losses.[52] This has significant implications for diamond-based betavoltaics, as diamond holds one of the highest band gaps of any semiconductor and thus would have a relatively high theoretical conversion limit.

Meanwhile, silicon, the most widely used semiconductor, has a band gap of 1.12 eV and is only thought to have a maximum conversion efficiency of 14%.[53] The lower radiation resistance of silicon also meant poorer operating lifetimes and efficiencies, making Si-based betavoltaics undesirable. Monte Carlo simulations of ^{63}Ni betavoltaic cells with GaN, SiC and Diamond Schottky diodes show conversion efficiencies of 16.8%, 22.0%, and 31.3%, respectively, highlighting the hierarchy of semiconductors.[54] Other theoretical studies gain similar conclusions, with the order of GaN and SiC being debatable, but one recurring conclusion is the superiority of diamond.[55, 56] One prominent issue within betavoltaics is the process of actualising the proposed theoretical efficiencies. GaN suffers harshly from this, with recent GaN betavoltaic cells possessing efficiencies within the 0.1-2% range, a far cry from its theoretical potential.[57-59] On the other hand, in 2016, high-efficiency SiC betavoltaics with record conversions of 18.6% have been demonstrated, getting much closer to the maximum.[60] GaN's shortcomings likely result from large numbers of defects present from the manufacturing process, and is also disadvantaged by its direct band gap, which does not couple as effectively with radioisotope sources.[55]

More importantly, a betavoltaic cell produced by Shimaoka *et al.* in 2020 using a diamond p-n junction has shown great success, achieving an ultrahigh conversion efficiency of 28%, the highest of any betavoltaic cell.[61] The 2020 paper utilises a p-n junction rather than an SBD as they have larger potential barrier heights of ~4.5 V (compared to ~2 V for diamond SBD). The lower barrier height of SBD reduces the efficiency drastically, resulting in ~60% of potential power conversion being lost for diamond SBD-based devices.[62] Furthermore, Delfaure *et al.* have utilised a diamond p-i-m junction to produce a betavoltaic cell with an outstanding open-circuit voltage and short-circuit current of 1.85 V and 7.12 μA, respectively.[63] These characteristics are unprecedented within Nickel-based betavoltaics, offering short circuit currents and open circuit voltages higher than those found in Si, 4H-SiC, and GaN cells.[64]

These results by Shimaoka *et al.* and Delfaure *et al.* highlight the prospects of which diamond betavoltaics cells can achieve. This prospect is also demonstrated by the diamond battery start-up companies such as Arkenlight and NBD, which have surfaced in recent years.[65, 66]

Meanwhile, diamond SBD betavoltaics have not met their full potential, being limited to conversion efficiencies of only a few percent.[1, 62, 67] Still, SBD-based betavoltaics cells produced by Bormashov *et al.* in 2015 showed much promise, even with a total conversion efficiency of 0.6%. The cell, made from 130 Pt/diamond diodes stacked together, had an output power density of 3 nano-Watts/cm^2, giving rise to a battery-specific energy of 120 mWh/g, a value competitive with chemical batteries.[1] In 2018, Bormashov *et al.* pioneered the field of betavoltaics, improving upon their previous design by stacking 200 SBDs in a more efficient pattern (Figure 8). The compact nuclear battery had outstanding output power densities of 10 micro-Watts/cm^3 and battery-specific energies of 3300 mWh/g, an order of magnitude higher than chemical batteries.[62]

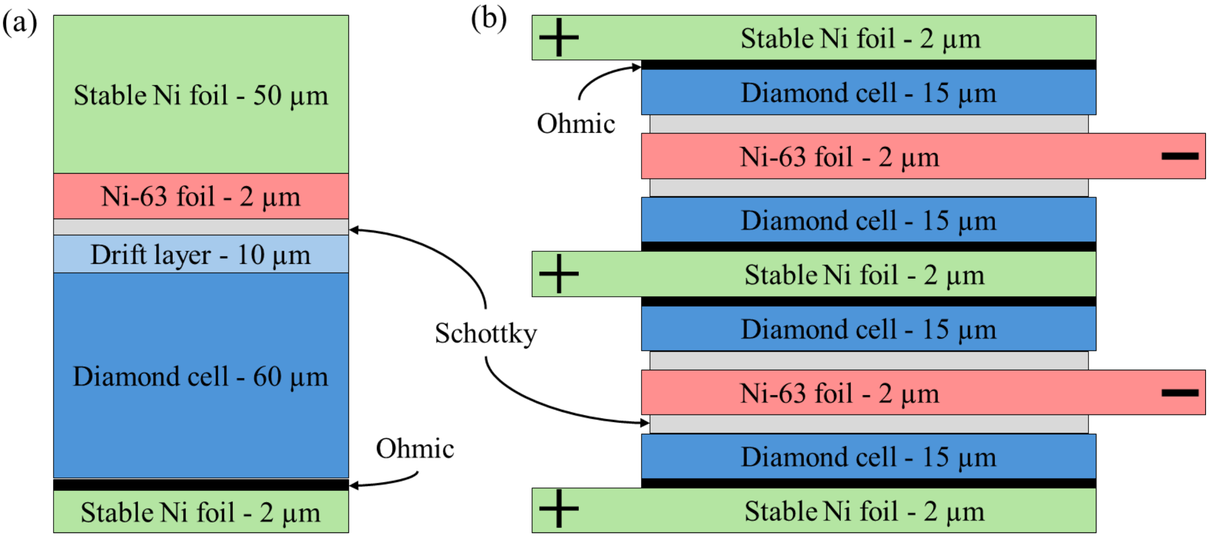

Figure 8. Diagrams of the two betavoltaic devices produced by Bormashov et al. (a) A singular cell in the nuclear battery prototype from 2015.[1] Low enriched Ni-63 was deposited electrolytically onto the stable Ni foil. Platinum Schottky contacts were employed between the Ni-63 source and the diamond while ohmic contacts of Ti/Pt/Au were made on the backside of the diamond substrate. The diamond cell had a less-doped drift layer which acted as the energy absorption region of the cell. (b) Cell packaging scheme for the revolutionary betavoltaic battery fabricated in 2018.[64] The cell uses ultra-thin diamond converters consisting of a low-doped drift layer (~15 µm) and the remains (<0.1 µm) of the heavily doped p$^+$ substrate. For the ohmic contacts the same metal mixture was used as in the 2015 cell while Ni was used for the Schottky contacts. Figure modified from Ref. 64

The first commercial betavoltaic cell utilised a radioactive promethium source and was used to power pacemakers in the 1970s.[68] Since then, most of the betavoltaics discussed in this review have opted to utilise ^{63}Ni as a radioisotope source for energy. In addition to its long half-life of ~100 years, radioactive nickel is commonly used as it is easier to handle than other sources (^{3}H, ^{90}Sr, and ^{147}Pm) and offers a lower energy beta spectrum that is suitable for less radiation-hard materials like SiC and Si.[69, 70] Strontium 90 (and ^{90}Y) offer one of the highest power densities of the beta decay sources but is incompatible for longer lifetimes due to severe displacement damage to the semiconductor from high-energy beta particles (Table 3).[71]

Table 2. Summary of key properties for betavoltaics of commonly utilised beta-emitters. Table modified from Ref. 74.

Radionucleotide	**^{3}H**	**^{63}Ni**	**^{14}C**	**^{147}Pm**	**^{90}Sr**
Decay energy /keV	18	67	156	225	540
Half-life /years	12	101	5730	3	29

While being lower than ^{90}Sr, Tritium (^{3}H) offers a high power density of roughly 50 times higher than ^{63}Ni with the added benefit of not damaging the semiconductor as heavily.[72] Furthermore, tritium is readily available as a nuclear waste by-product and can easily be incorporated into various metals and organic compounds to act as solid sources of beta decay.[73] Titanium tritide is a common solid source for tritium-based betavoltaics as it offers a higher ^{3}H density than the gas form, allowing for a higher beta ray density and more power.[74] Tritium betavoltaic cells have already been commercialised by City Labs, utilising a tritiated metal hydride foil and semiconductor p-n junction.[75] However, with solid tritium sources, self-absorption of the beta particles is a common issue that hinders betavoltaic power outputs and conversion rates. Li *et al.* deduced from simulations that the power emitted from Titanium tritide films that were 0.7 µm thick had negligible differences when compared to thicker films, citing self-absorption as the main cause.[76] This is not specific to only tritium, as Monte Carlo simulations of ^{63}Ni beta particle transport have also shown self-absorption to be the major cause of efficiency loss, demonstrating it to be a critical issue within betavoltaics.[77] Furthermore, within low-output sources (^{3}H, ^{63}Ni, and ^{14}C), carrier recombination was also found to be a major contributor towards efficiency loss, an issue that is somewhat addressed by the use of wider band gap semiconductors like diamond.[78]

To address these limitations, semiconductor material that can integrate the betavoltaic sources within themselves, and thus reduce self-absorption, have been researched upon. Chepurnov *et al.* have proposed such a device, utilising a nano porous SiC substrate implanted with ^{14}C as a radioactive source.[79] Similar to tritium, Carbon 14 is a purely beta-emitting source that is readily available as it is a large by-product of graphite-moderated nuclear reactors.[80] Although ^{14}C lacks similar power densities to ^{3}H and ^{63}Ni, its shortcomings are superseded by its extremely long half-life of 5,730 years.[72] Moreover, ^{14}C has the unique ability to act as both the beta source and electrode due to its highly conductive properties. This was first demonstrated in 2020 by Hwang *et al.* who developed a dye-sensitised betavoltaic cell where ^{14}C simultaneously acts as the beta emitter and a counter electrode.[81] Additionally, with the recent technological developments within the diamond industry, self-glowing diamonds incorporated with radioactive ^{14}C have been grown by HPHT.[82] This opens up the possibility for creating semiconductor-based betavoltaics using radioactive diamond as both the beta source and the diode converter. This significant milestone was reached in December 2024 by the UK Atomic Energy Authority and the University of Bristol, who have developed the first ^{14}C battery, which has the potential to provide power for thousands of years (Figure 9).[83]

Figure 9. The radio luminescence of the synthetic ^{14}C diamond film developed by the University of Bristol and the UKAEA. The weak luminescence was captured using a low light intensity camera. Image taken from Ref. 85

However, the decay process of the ^{14}C atoms can have long-term effects on the electronic properties of the material. The beta-minus decay process involves the conversion of a neutron to a proton; when a ^{14}C atom undergoes beta decay, it transforms into a ^{14}N atom. This substitution can have consequences for the properties of the bulk diamond due to changes in lattice constants. A density functional theory (DFT) computational study of ^{14}C diamond performed by Li *et al.* has shown that the conversion from ^{14}C to ^{14}N has a strong influence on the band gap. Depending on the configuration of new lattice, the material can exhibit metallic behaviour or act as an indirect band gap semiconductor.[84] Therefore, a ^{14}C-^{12}C betavoltaic cell can exhibit p-n or Schottky junction characteristics depending on the new configuration which occurs. While the addition of N to the lattice reduces the stability, the short circuit current of the cell seems to increase, with the more stable configurations resulting in lower band gaps for the system. This transformation seems to work in favour of ^{14}C betavoltaic cells, adding donor impurities as the decay process occurs, but due to ^{14}C's long half-life, it will be difficult to utilise this practically. Furthermore, ^{14}C batteries are still in their infancy, requiring further research and development to be established commercially.

3. Tritium Batteries

3.1 Hydrogen within diamonds

Building upon the idea of radioactive diamond betavoltaic cells, tritium is another source which can be incorporated into the diamond lattice. Infra-red absorption spectra of natural diamonds have shown hydrogen to already be a major impurity found within defects of the crystal.[85] The majority of the hydrogen is found within proximity to the surface, acting as a termination for the 'dangling' bonds found at the ends. Interestingly, the sub-surface (deeper than 4000 Å) concentration of hydrogen remains almost constant throughout, being in the range of 100-1000 ppm (~10^{19} to 10^{20} atoms).[86] Just how this hydrogen is incorporated into the diamond remains under debate, with IR spectra showing conflicting results of covalently bound hydrogen between sp^3 and sp^2 hybridised stretching modes.[87] Furthermore, by the use of muonium models, hydrogen (and H_2) is also thought to be able to occupy multiple interstitial positions, each with different symmetries.[88, 89] While this hydrogen incorporation can have adverse effects on the electronic properties of the diamond, it also opens the possibility of incorporating tritium into the diamond bulk as a beta source.[90] This opportunity is present for various materials but is especially advantageous for diamond as it is deemed to be one of the most optimal semiconductors used to convert tritium decay energy.[55]

When compared to natural diamonds, synthetic HPHT diamonds show similar but slightly higher hydrogen concentrations ($[H_2]$) ranging from roughly 8×10^{19} to 1.6×10^{20} atoms per cm^3 (450-900 ppm) in the bulk.[91] Meanwhile, CVD grown diamonds would be expected to have much higher hydrogen contents due to their high $[H_2]$ growing environments of ~95-99% being much higher than the $[H_2]$ found in the earth's crust or HPHT.[92] However, this does not seem to be the case, with Dischler *et al.* observing MWCVD grown polycrystalline diamond (PCD) films to have hydrogen contents between 4000-9000 ppm (8×10^{20} to 1.6×10^{21} atoms per cm^3), only an order of magnitude larger than values reported for natural and HPHT diamonds.[87, 91] Additionally, analysis of $[H_2]$ in diamond-like carbon shows similar results, where CVD films grown under a 75% hydrogen gas mix had only 4% more $[H_2]$ than a film grown under 25% hydrogen.[93] The results demonstrate that increasing the $[H_2]$ in the CVD growing atmosphere does not necessarily correspond to higher hydrogen content and is thus not an effective technique for the hydrogen loading of diamonds.

As touched upon briefly, a higher incorporation of hydrogen into the diamond could result in adverse effects on the properties of the crystal. Haque *et al.* noted that arc-jet deposited diamonds with higher hydrogen contents displayed darker colours.[94] With these darker diamonds, a larger full-width at half-maximum value was also observed for the diamond Raman peak at 1332 cm^{-1}, implying a poorer quality diamond. To supplement these findings, Tang *et al.* suggest that the hydrogen content of diamond films correlates with the crystalline and phase quality, where diamond films that suffer from secondary nucleation or an increase of non-diamond components have higher hydrogen incorporation.[95] The aforementioned experiment by Dischler *et al.* shows that, apart from at the surfaces, hydrogen is predominantly found within grain boundaries and dislocations within the crystal.[87]

3.2 Difficulties of using tritium

It is important to distinguish the difference between hydrogen and its isotopes. While a hydrogen atom consists of only a single proton (and electron), the deuterium and tritium atoms contain one proton (and electron) with one and two neutrons, respectively (Figure 10). Other than causing the nucleus to become unstable in tritium, these extra neutrons increase the mass and size of the atoms, possibly influencing the way in which they interact with the diamond lattice. Therefore, tritium, deuterium, and hydrogen might not interact in identical ways during diamond incorporation. This introduces further challenges to evaluating tritium incorporated diamond batteries, being the risks and elusiveness associated with the radioisotope.

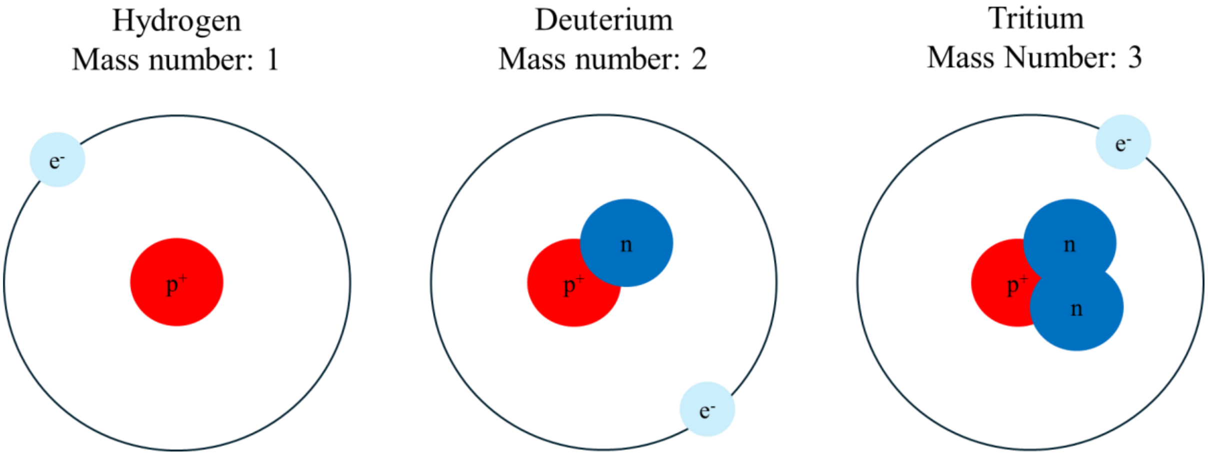

Figure 10. The three most stable isotopes of hydrogen. Protium (A = 1) is commonly referred to as just hydrogen. Hydrogen is the most common isotope, with an abundance of >99.98%. While hydrogen and deuterium are stable, tritium is unstable with a half-life of ~12 years.

In the atmosphere, tritium is produced by nuclear reactions of gaseous atoms with cosmic rays at an approximate rate of 0.12 atoms cm^{-2} s^{-1}.[96] Much of this tritium produced in the atmosphere is absorbed into oceans and various bodies of water, forming tritiated water (HTO). A miniscule amount of tritium is also found in the earth's crust from the decay processes of lithium-6, uranium and thorium occurring in the rock. This formation has a production rate of ~0.001 atoms cm^{-2} s^{-1}, which is evidenced by the presence of the isotope helium-3 in igneous rock.[96] With these processes combined and by factoring in the half-life of tritium (~12 years), the natural tritium inventory is thought to consist of around 2800-3500 grams (1-1.3 EBq), with 99% present in the water cycle as HTO.[97] However, it would be remiss to not discuss the artificial production of tritium, especially as a by-product of nuclear reactors, where most of the tritium utilised for betavoltaics would theoretically be sourced from. In light water reactors (LWR) tritium is produced from thermal neutron irradiation of helium-3 or lithium-6 and by the fast neutron bombardment of boron-10, nitrogen-14, and lithium-7.[98] Tritium is also the dominant radioisotope present in releases from heavy water reactors (HWR), resulting from neutron capture of the deuterium present in the water. A single CANDU-type HWR is said to generate between 100 and 200 grams of Tritium a year, with 90% of this being in the form of tritiated heavy water.[99] As the tritium required in a betavoltaic device would be negligible compared to the amount produced by the dozens of HWRs around the world, the supply of tritium is not a concern.

The issue instead stems from the difficulty of refining and containing tritium, whose propensity for leaking makes it the radioisotope with the highest exposure rate (for electricity generation-related radiation) around the world.[100] Still, many tritium removal facilities (TRFs) exist, with the most prominent being the Wolseong TRF in South Korea (Figure 11).[101] Guided by the prospects of fusion energy, more facilities are being developed, such as the Cernavoda TRF in Romania and the tritium research facility, H3AT, by the UKAEA.[102, 103] Aside from radiation exposure, TRFs raise further safety concerns as the radioisotope is a crucial component in boosted fission bombs, which require only a few grams of the isotope. This concern is justified, as commercial reactors, such as the Savannah River TRF in the US, have already been used to produce tritium for military purposes.[104] Due to this, any production of tritium is regulated, making it difficult to acquire the isotope and resulting in tritium being one of the most expensive substances by weight. With these considerations in mind, the use of tritium in experimental contexts of batteries seems too costly and hazardous, therefore, opting to use deuterium, the isotope of hydrogen closest to tritium, is a reasonable alternative. Additionally, comparison between deuterium and hydrogen could highlight possible differences resulting from a change in the mass of the atom, which can be extrapolated towards tritium.

Figure 11. The Sizewell B nuclear power station (left) is the only commercial LWR in the UK. The reactor stores its spent fuel and waste in underwater and dry cask storages. The Wolseong nuclear power plant (right) hosts four CANDU reactors and the Wolseong TRF, which processes and removes the tritium in the heavy water used as reactor coolant. Figures taken from public domain, *via* Wikimedia Commons.

3.3 Investigation into deuterated diamonds

Experiments by growing single crystal diamond (SCD) homoepitaxially in a deuterium/methane atmosphere (1.5% CH_4 in deuterium) have yielded surface deuterium concentrations of 1.70×10^{15} atoms per cm^2 and a bulk deuterium and hydrogen content of roughly 1.0×10^{19} atoms per cm^3 at depths below 1.5 nm.[105] Although the surface deuterium content is similar to those reported for hydrogen-grown CVD diamonds, the bulk concentration corresponds to roughly 50 ppm, being much lower than the usual hydrogen content of the diamond bulk.[91, 106] Mizuochi *et al.* reported higher quality diamonds from CVD growths in a deuterium-rich atmosphere due to an increased suppression of point defects within the lattice.[107] A higher etching rate of ~30% was also observed for the deuterium mixture when compared to hydrogen. Bogdanowicz *et al.* observed that growing BDD using a deuterium-rich environment (99/1/0.005, $D_2/CH_4/B_2H_6$) resulted in higher doping concentrations, with less sp^2 phases and C-H defects being found.[108] While this is an improvement towards achieving higher doping concentrations, the lower number of defects could result in a lower bulk deuterium incorporation as hydrogen is found to incorporate into the defects in CVD diamonds.[109] Furthermore, as the growth took twice as long to achieve the same film thickness as in a hydrogen environment, growing diamonds in a deuterium atmosphere might not be suitable for tritiated diamond betavoltaics.

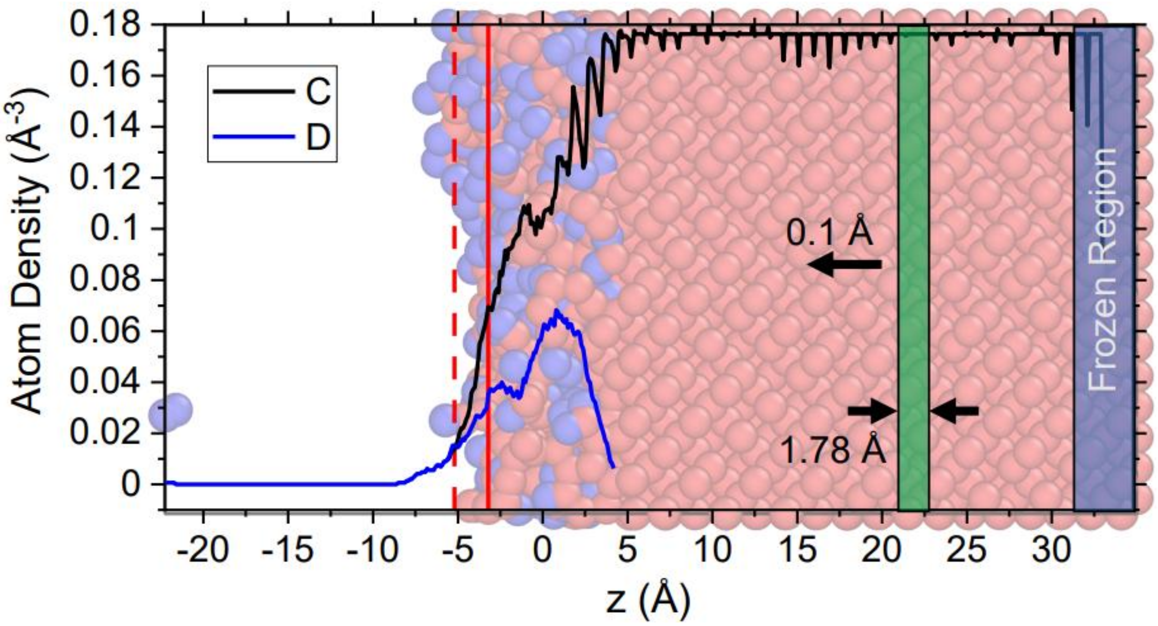

Figure 12. A render taken partly through simulation of diamond being bombarded by deuterium atoms modelled by Pittard et al.[113] The red line represents the surface of the diamond, with the dashed line showing the cut-off point, beyond which ions were not measured. The black and blues lines represent the atom densities carbon and deuterium. The implanted deuterium atoms are seen to congregate around the surface, not breaching into the bulk of the diamond. Figure taken from Ref. 113

Another option that is utilised frequently is the ion implantation of deuterium into diamond (Figure 12). During ion implantation, deuterium ions are accelerated across potential differences and, upon hitting the diamond, are implemented into the lattice. The potential differences that they are accelerated with can have an impact on the number of ions embedded into the substrate, with higher energy correlating to better ion retention.[110] That being said, ions of sufficiently high energy can damage the crystal structure, so a fine balance is required. One advantage which ion implantation has over the passive incorporation of CVD is that the higher energy particles can incorporate into areas with higher energy barriers. These areas being outside of grain boundaries and defects, which are difficult for lower energy particles to occupy. This was observed by Pittard *et al.* in the thermal desorption spectroscopy (TDS) for diamonds bombarded with deuterium, where a second D_2 peak appears at higher temperatures. This second peak is not seen for HD and H_2, suggesting the deuterium had embedded itself in a higher energy position which hydrogen could not, with the likely candidate being inter-grain binding sites.[111] However, ion implantation is limited to penetration depths proportional to the energy, with deuterium ions with an energy 1000 eV not being able to successfully penetrate towards the depths where hydrogen is observed. Furthermore, molecular dynamics studies done by Pittard *et al.* show that deuterium ions with energies of 140 eV have max penetration depths of 5 nm, not being sufficiently deep enough for bulk loading of diamond.[111]

Within diamond and other conventional semiconductors, hydrogen can diffuse deep into the bulk during CVD growth. If this diffusion can be replicated outside of the CVD process, a method to incorporate deuterium deeply into diamonds can be achieved. Ballutaud *et al.* investigated the diffusion characteristics of deuterium in diamond by exposing undoped PCD to deuterium plasma.[112] The diamond samples were initially annealed at 1200 °C in an ultra-high vacuum to remove hydrogen present from the CVD process. After two hours of exposure to either a deuterium radiofrequency plasma at 500 °C or a deuterium microwave plasma at 800 °C, the diamonds demonstrated deuterium depth profiles up to a few hundred nanometres. The radiofrequency plasma showed the most promising depth profile, recording deuterium concentrations of roughly 1×10^{17} atoms per cm^3 (~1 ppm) at 600 nm deep in the bulk.[112] Yet again, the deuterium diffusion was found to be mainly governed by the defects found within the polycrystalline structure of the diamond.

Deuterium diffusion experiments on BDD show more promise, demonstrating high deuterium concentrations of 300-600 ppm (~10^{19} atoms per cm^3) at depths up to ~750 nm.[90] This increase is proposed to be due to the formation of stable boron-deuterium pairs, which are also seen to passivate the boron acceptors.[113] These retention values are comparable with the concentration of hydrogen found within natural diamonds, with higher boron doping concentrations corresponding to higher diffusion depths. Other deuterium diffusion studies on BDD have demonstrated similar extents of deuterium loading, also showing higher plasma temperatures to correlate with higher concentrations.[114, 115] Within these experiments, the deuterium concentration with respect to depth falls off much faster for monocrystalline samples rather than polycrystalline, further supporting the role of defects and grain boundaries within deuterium loading.

4. Aim of thesis

Due to the high potential demonstrated by deuterium diffusion experiments, this thesis aims to investigate the potential of tritiated diamond betavoltaics by loading various diamond samples with hydrogen and deuterium in a heated gas environment. The diffusion runs will be performed with hydrogen and deuterium gas to determine if any differences arise from the change in isotope and thus extrapolate those findings towards tritium. Different diamond samples will also be used to determine the effect of defects and grain boundaries on the concentration of deuterium implemented into the diamond to determine the most suitable diamonds for tritium betavoltaic applications.

5. Experimental

5.1 Overview

To determine the efficacy of thermal diffusion, various samples of differing morphology had to be analysed. Both boron-doped PCD (BDPCD) and boron-doped SCD (BDSCD) samples were utilised to investigate whether the number of grains and boundaries would influence hydrogen isotope retention. Additionally, a pristine SCD sample of which roughly three-quarters was graphitised was also used, with the non-etched section acting as a pristine control.

After an initial hydrogen run with a PCD sample, multiple samples of varying types were loaded with deuterium. After the loading process, samples were placed onto specifically designed quartz ‘boat’ vessels, which were pushed into the tube furnace. The furnace was set to ramp up to 1000 °C and hold for four hours. After the diffusion process, the samples were re-weighed, and the surface was analysed further *via* the LEXT laser microscope and Raman spectroscopy. Subsequent analysis into deuterium and hydrogen content was done through secondary ion mass spectrometry (SIMS), with one BDSCD sample being analysed using TDS.

5.2 Sample Preparation

Freestanding BD PCD and pristine SCD films were sourced from Element6 (Ascot, United Kingdom). The BD PCD were 9 mm by 5 mm and 0.35 mm thick, while the pristine SCD chips were 6.8 mm by 3.3 mm and 0.2 mm thick (Figure 13). Both films were grown using CVD and laser cut to their respective sizes. The surface roughness of the BDPCD was left as grown, while the SCD was polished to an average roughness of less than 30 nm.[116]

Figure 13. Image of the three types of samples investigated. The freestanding BDPCD (left) is larger than the other samples and is fully boron doped. The BDSCD (middle) is a pristine diamond with a thin boron doped layer grown using a CVD reactor. The graphitised SCD (right) uses the same base as the BDSCD but has been laser cut using the laser micromachining tool in the diamond lab.

To produce a BDSCD, a boron-doped layer was grown on top of the pristine SCD using the ASTEX-type MWCVD reactor in the diamond lab (Figure 14). The growing conditions are listed in Table 4 and correspond to a gas mixture of 99% H_2 with a ~0.25% boron concentration relative to carbon, considered a high doping concentration. The gas flow rates were controlled using mass flow controllers (MFC) and were measured in standard cubic centimetres per minute (SCCM). Plasma was initially struck at a microwave power and pressure of 0.7 kW and 15 torr, respectively, after which the pressure and power were increased in tandem, maintaining a power and pressure (kW:torr) ratio of 100 until growing conditions were reached. H_2 was flowing throughout the striking process, while methane (CH_4) and diborane (B_2H_6) gas were only enabled after the system reached 50 torr. The diborane gas used for the growth consists of 5% w/w% B_2H_6 in H_2. Previous calibrations done in-house suggest the growth rate of diamonds in a high boron atmosphere to be around 1.5 µm/hour; therefore, the doped layer is expected to be less than a micron thick after 30 minutes of growth.

Table 3. The CVD growing conditions were used for the boron doped layer on the BDSCD sample. Temperature was measured using a pyrometer

Power	Pressure	Temperature	Time	[H_2]	[CH_4]	[B_2H_6]
1000 W	100 torr	925 – 975 °C	30 min	300 SCCM	12.5 SCCM	0.7 SCCM

On a different pristine SCD, graphitised regions were introduced into the diamond *via* the use of an Oxford Lasers (Oxfordshire, United Kingdom) Alpha 532 laser micromachining tool (Figure 15). The machine uses a diode-pumped nanosecond laser with a wavelength of 542 nm.

The laser spot is ~5 micrometres in diameter and can reach powers up to 5 W at 10 kHz. Fifteen digits were etched into the surface, each digit being 4500 µm long with a thickness of 20 µm. To help the laser focus on the transparent sample, a marker was used to black it out before the etching process. Etching of the surface using such a laser is shown to result in graphitisation, inducing defects and converting the diamond into graphitic carbon.[117]

Each sample was weighed before and after hydrogen/deuterium loading to determine whether the loading process would result in a change in mass, either from the etching of the sample or through implantation of hydrogen/deuterium atoms. The weighing was done on a five-decimal gram scale with a detection limit of 0.01 mg. The weighing process was done in the synthetic laboratories at the University of Bristol, where the specific five decimal scale is housed.

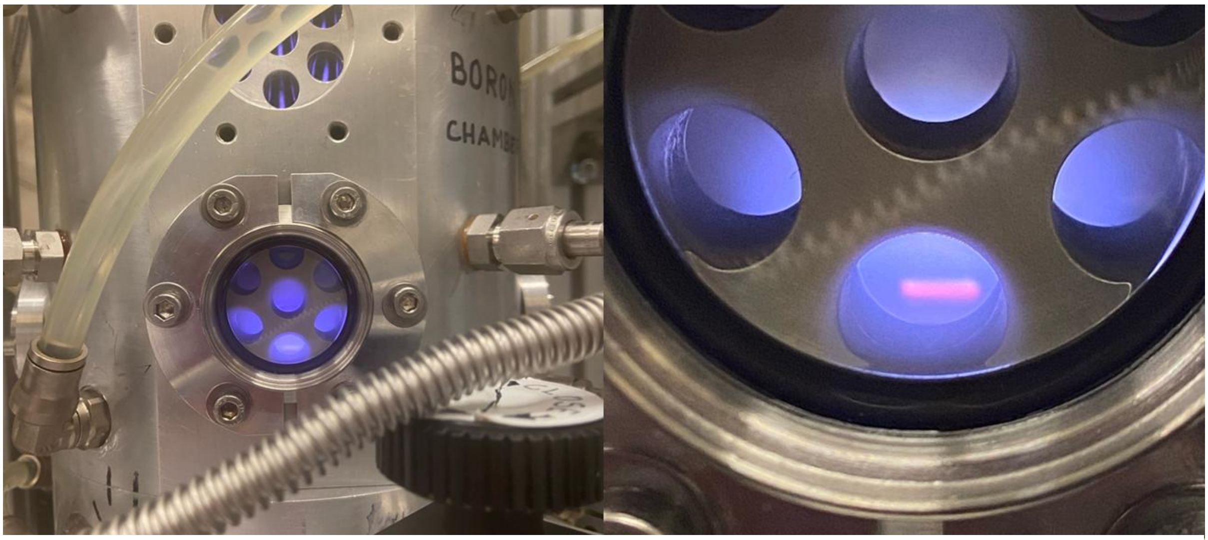

Figure 14. The ASTEX-type CVD reactor during growth of a diamond. The plasma is observed to be purple due to a mixture of CH_4 and H_2 gas. During boron doping, an orange halo is typically observed at the top of the plasma. The diamond can be seen glowing red hot due to the high temperatures involved in the process.

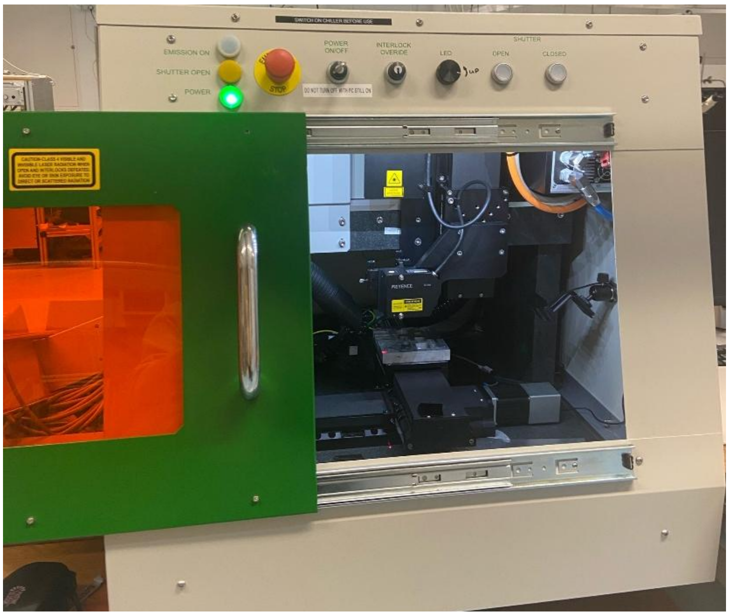

Figure 15. The Laser Micromachining tool at the diamond lab. The apparatus is commonly used to cut or etch at diamond and other hard materials.

5.3 Configuring the Tube Furnace

A Nabertherm (Bremen, Germany) compact tube furnace (Figure 16) was used for the heating process. The furnace had to be configured and adjusted to be suitable for hydrogen and deuterium loading applications. The furnace has a maximum temperature of 1200 °C and is designed for laboratory use in under atmosphere and vacuum conditions. The furnace was also fitted with a long quartz tube for samples, which was designed for low pressure use. Metal-quartz tube fittings had to be adapted at the glass workshop in the University of Bristol Chemistry Department to form glass joints between the quartz tube and Swagelok tubing for gas and vacuum.

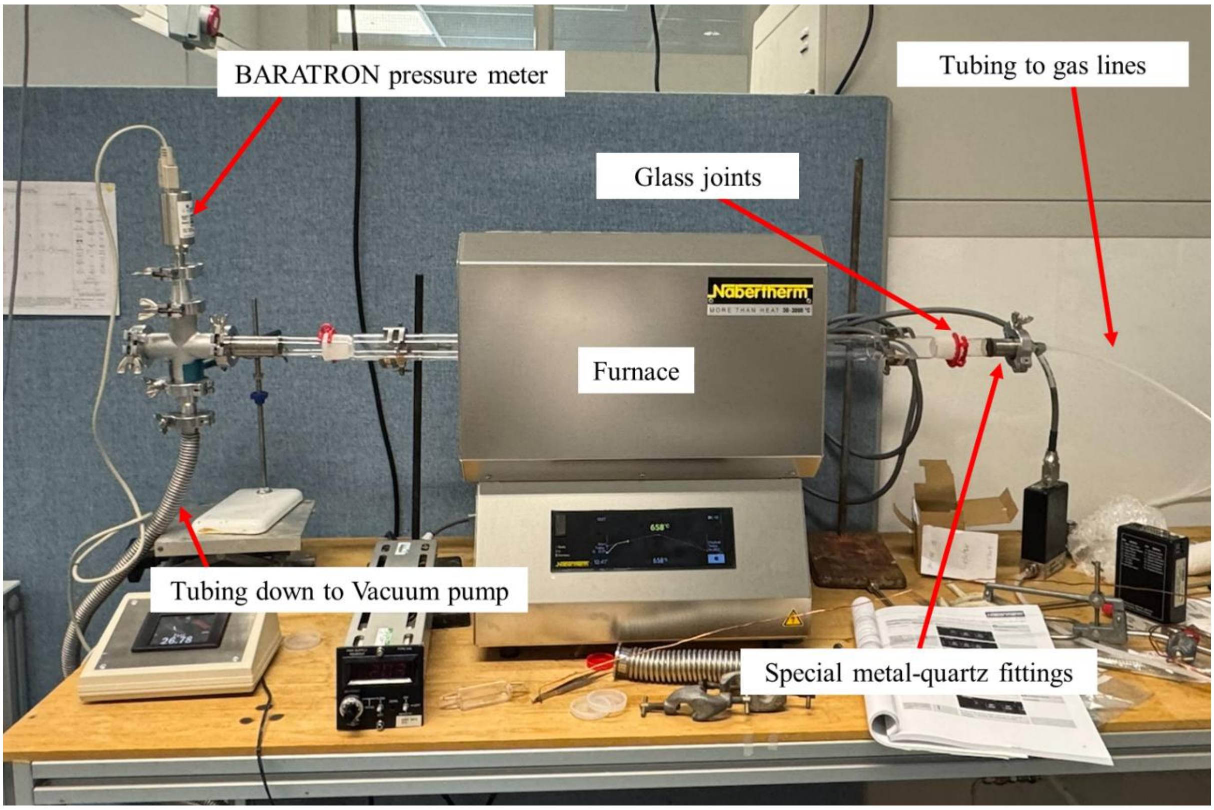

Figure 16. Annotated image of the initial setup used for the Tube Furnace; improvements were added after leak testing**.** Photograph taken in October by Gurjosh Barn, another student at the diamond lab.

To control and regulate the pressure within the system, the tube furnace was fitted with two pressure monitors, a BARATRON pressure transducer (MKS instruments Ltd., Massachusetts, United States) for high pressure measurements and a THERMOVAC TM 101 (Leybold GmbH, Cologne, Germany) was added later for low pressure readings. The system was also rigged with a Burkert flow controller, where a valve leading to the vacuum pump could be adjusted to control the overall pressure of the system.

5.4 Leak Testing and Proofing of the Furnace

Upon previous runs performed by another student, diamond samples in a heated nitrogen atmosphere exhibited heavy etching, suggesting an oxygen leak was present in the system. When left under vacuum (~10 torr) and isolated from the pump, the system experienced an increase in pressure from 30 torr to 50 torr in roughly six minutes. Nitrogen was flowed through the furnace at 5 and 10 SCCM, leading to pressures increasing from 30 to 50 torr in 230 and 155 seconds, respectively. As both measurements will have the same baseline leak rate, it was determined that a leak rate of 5 SCCM corresponded to an increase from 30 to 50 torr in 75 seconds. From this, the initially observed six-minute leak rate corresponded to a leakage of ~1 SCCM, being deemed unsuitable for an H_2 run.

Through repeated leak experiments isolating different parts of the system, the majority of the leak was found to result from the glass joints of the quartz tube. PTFE plastic was subsequently applied around the joints to provide a better seal. Upon further reconfiguration to reduce strain on the glass joints with the PTFE, the system took 668 seconds to go from 30 to 50 torr, corresponding to a leak rate of 0.56 SCCM. This rate was deemed satisfactory to proceed with a test run using H_2 gas.

5.5 Etching Test Run

To ensure samples would not be etched too heavily, a scrap polycrystalline BDD was used for a test run. The sample was inserted into the quartz tube, and the system and gas lines were evacuated of all gas. The hydrogen line was fitted to the tube furnace with a TYLAN 2900 (Merck Millipore, Massachusetts, United States) mass flow controller (MFC), allowing for the flow rate of H_2 to be controlled. The H_2 MFC is controlled in terms of percentages of the maximum flow rate, being 250 SCCM; therefore, a setting of 0.6 would correspond to a flow rate of 150 SCCM.

The system was subsequently purged under a 250 SCCM flow of hydrogen, with the vacuum valve set to its maximum (73.0% open). The valve position was set to be 54.0% open, after which pressure stabilised within a range of 350-400 torr. The heating program was started at room temperature and took 40 minutes to reach 1000 °C. Due to the thermal expansion of the gas, the valve had to be opened to 55.5% and 58.2% at 500 and 1000 °C, respectively. The system was left to cool down overnight, and the sample was retrieved. Upon initial inspection, the sample seemed to be undamaged, with tape markings from previous uses still present on the diamond.

5.6 Hydrogen Loading

After the test run, the quartz tube was fitted with fused glass joints (Figure 17), which improved the leak rate of the system and allowed it to reach a vacuum as low as 7×10^{-2} mbar. With the improved quartz tube, the freestanding boron-doped PCD was chosen for the first hydrogen loading run. The diamond was placed into a specially designed quartz boat (Figure 18) and was pushed in using a long metal rod. The system was left to pull a vacuum overnight, resulting in a base vacuum of 7×10^{-2} mbar recorded before the run. The system was then purged with a high flow (100 SCCM) of hydrogen for roughly two minutes to bring it up to a pressure of ~350 torr, after which hydrogen flow was set to 10 SCCM.

After pressure stabilised around 350 torr, the tube furnace was set to ramp up to 1000 °C. The system took roughly 40 minutes to heat up to 1000 °C, after which it remained stable, fluctuating between 994 and 1006 °C. When setting up the system, the program was set to stay at 1000 °C for four hours. However, the program did not account for the ramp-up time, so the sample was only exposed to a 1000 ± 6 °C atmosphere for around 3 hours and 20 minutes. The system was left to cool down overnight, after which samples were taken out and stored for analysis.

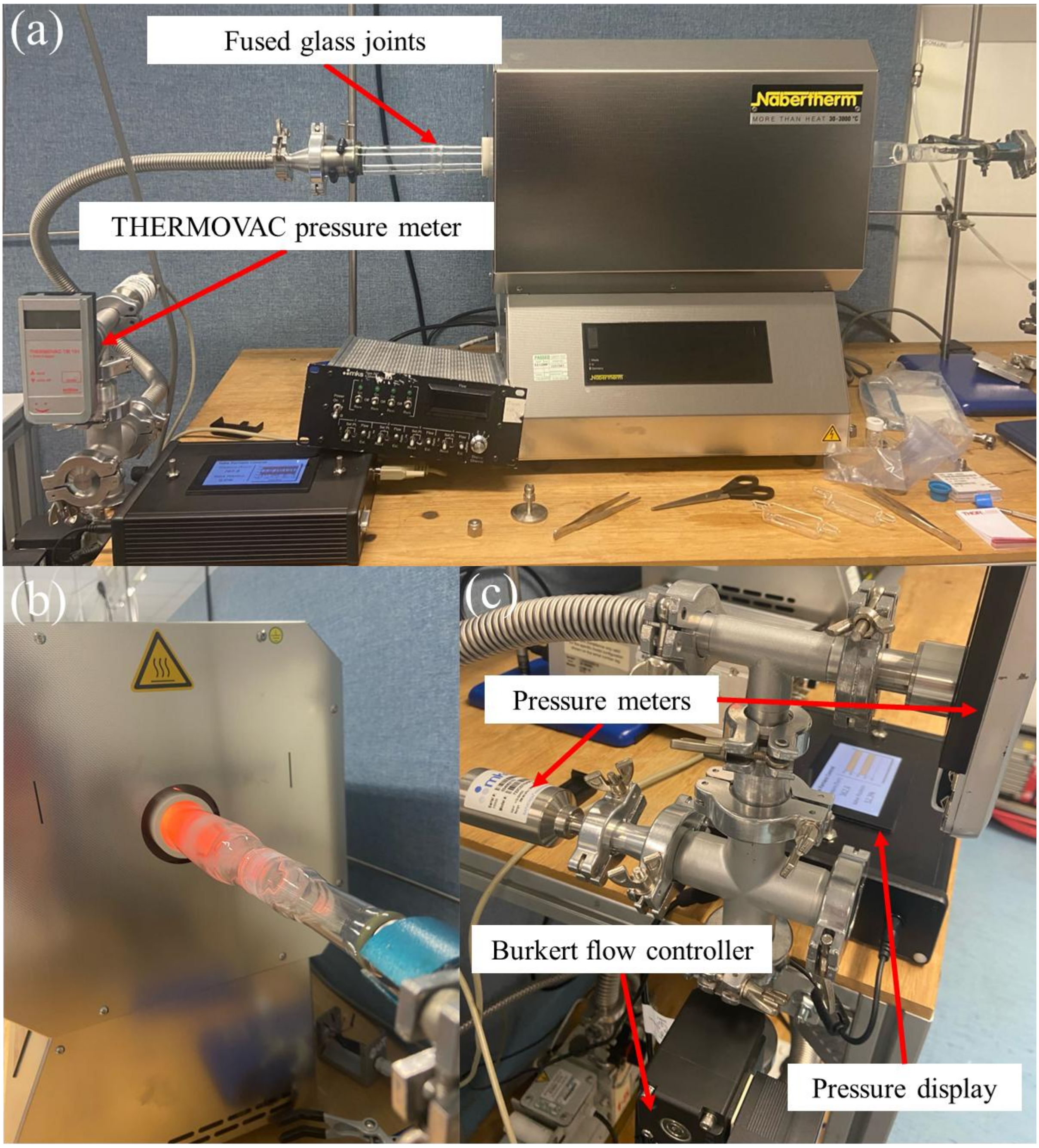

Figure 17. Image of (a) the final configuration used for the tube furnace with the addition of the THERMOVAC pressure meter and the fused glass joints to reduce leakage. (b) The tube furnace during a loading run exhibiting the orange glow of the high temperature interior. (c) Close-up of the new configuration showing the two pressure meters, the pressure display and the Burkert flow controller.

5.7 Deuterium Loading

Upon doing the hydrogen run, the loading program was adjusted so that the furnace was set to stay at 1000 °C for four hours after completing the first step of reaching 1000 °C, addressing the previous issue. Samples were placed onto the quartz boat and pushed into the tube using a long metal rod. The system was pumped down overnight, leading to a base vacuum of $\sim 7 \times 10^{-2}$ mbar. Deuterium gas was drawn from a 100-litre cylinder, pressurised at 19.4 bar. The cylinder was sourced from BOC Limited (Woking, UK) and connected to the previously used hydrogen gas line. The lines and system were purged, and Deuterium flow was set to 5 SCCM.

The loading program was initiated, and deuterium flow had to be increased (~20 SCCM) during ramp-up to reach a stable pressure of ~350 torr, after which it reduced back to 5 SCCM. After 40 minutes, the program reached 1000 ± 6 °C and maintained the temperature for four hours. The valve was set to 54.8% open to maintain ~350 torr and was opened further to 54.3% during the program. Once the program had finished, deuterium flow was left on until the system had cooled down to below 600 °C to prevent implanted deuterium from diffusing out.

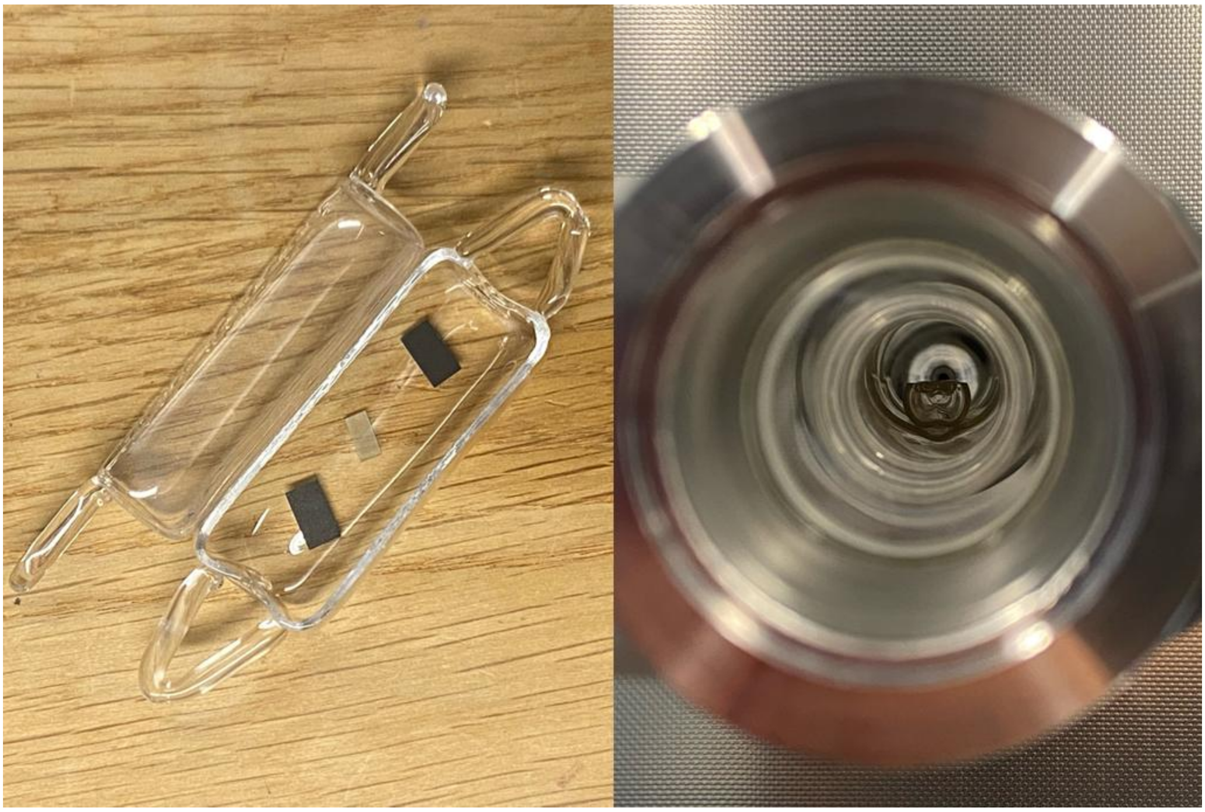

Figure 18. Demonstration of how the samples were placed into the furnace on quartz boats (left) which were designed in house and produced at the glass workshop. The image on the right shows the boat with the samples inside the quartz tube, which would be sealed and evacuated of air before the loading process.

6. Characterisation and Analytical Techniques

6.1 LEXT laser microscope

A LEXT OLS5100 laser microscope from Evident Scientific (Tokyo, Japan) was used to observe and analyse the surface of each sample (Figure 19). The LEXT microscope is capable of magnifications up to 100x and can perform 3D analysis of surface morphologies. 2D and 3D images were taken of each sample, and the 3D scans for each sample type are presented below in Figure 20. Samples were also analysed under the microscope before and after the loading to determine whether samples had been etched by the process.

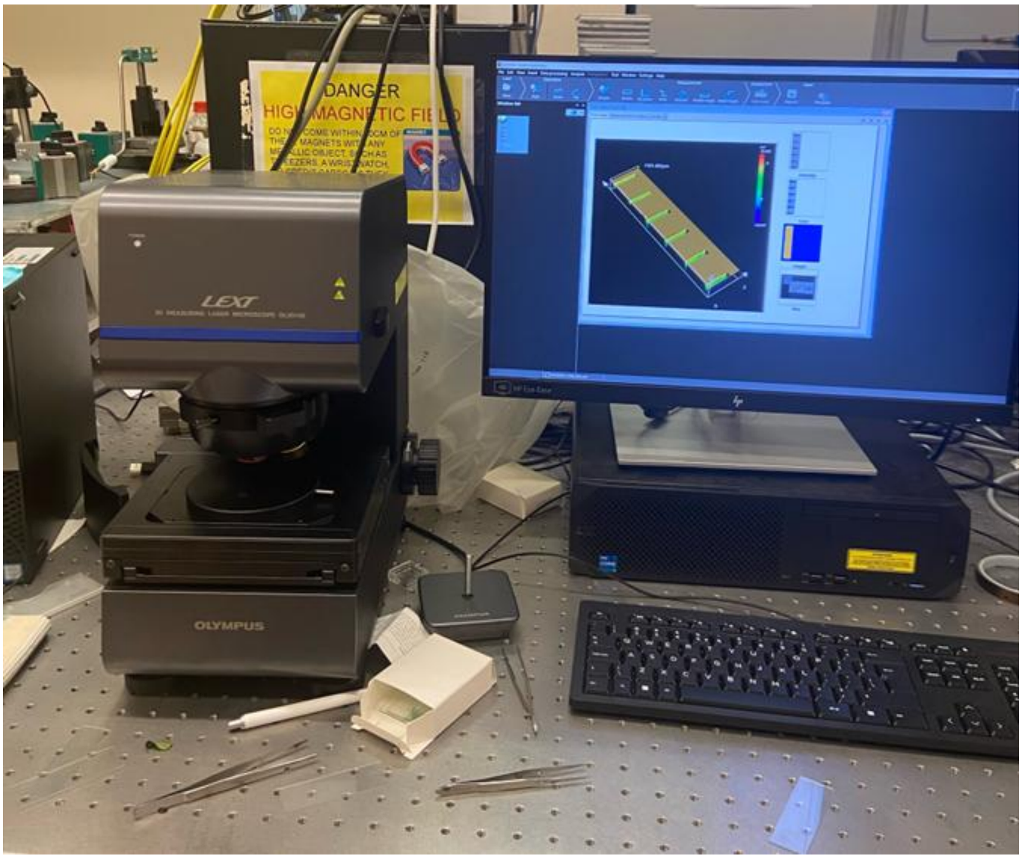

Figure 19. The LEXT OLS5100 laser microscope in the diamond lab. The instrument was used for analysis of surface morphologies as well as magnified 3D imaging of samples.

6.2 Magnification and 3D imaging

Under the microscope, the freestanding BDPCD (Figure 20.a) had numerous defined grains whose sizes are in the tens of microns. Due to this, the sample could be considered 'microcrystalline' exhibiting larger grains than nano- or ultrananocrystalline diamonds, which have grain size in the nanometre scales.[29] As discussed previously, the boundaries between these grains could host binding sites and defects to house extra deuterium, possibly increasing retention.[111]

On the other hand, the BDSCD consists of a single, flat grain without any large ridges, valleys or imperfections. There does seem to be some noise present on the surface, likely due to the low level of magnification used for the scan. Without having any grain boundaries, the sample is expected to hold less deuterium than its polycrystalline and etched counterparts.

The LEXT system was also able to analyse the laser etching of the graphitised sample (Figure 20.c). 3D analysis of the digits shows maximum etching depths of ~90 µm, which seem to get shallower across the sample. The etched regions are expected to contain graphitic carbon with a large number of defects that can house deuterium. Intriguingly, the graphitised SCD seems to have small imperfections, being bumps and divots, on the unetched regions, possibly as a result of the etching process.

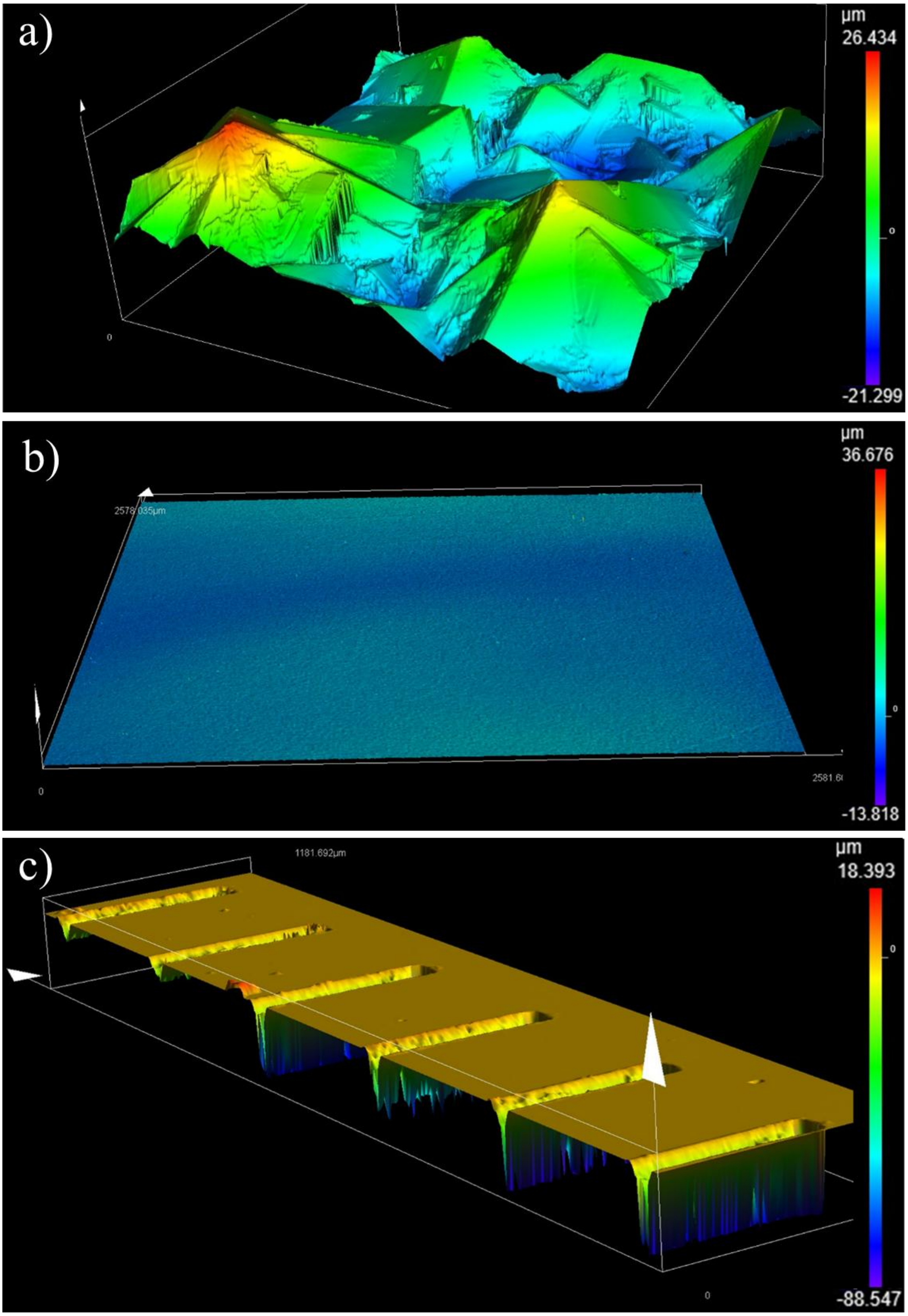

Figure 20. LEXT analysis of (a) the freestanding BD PCD sample from Element Six taken at ×100 magnification. The various grains and their boundaries are prominent, and the average grain size is determined to be in the 10s of microns, suggesting the diamond is microcrystalline. (b) The BDSCD grown in the diamond lab, taken at ×10, is seen to be quite flat and uneventful. (c) The graphitised SCD taken at ×20, showing the regions etched using the laser micromachining tool. The etched troughs seem to get shallower when moving down the sample.

6.3 Depth measurements

On top of imaging, the LEXT was used for more through-depth profiling of samples. This process was done for the etched regions on the graphitised SCD to properly quantify the depth of the regions. The process was also done for the flat SCD samples post-SIMS analysis to gain an understanding of the etching rate of the SIMS instrument. These depth profiles are presented in Figure 21 below.

The etched digits on the graphitised SCD are seen to vary in depth throughout the sample (Figure 21.a). Focusing the laser onto a transparent sample, such as the pristine SCD, is difficult, requiring marking of the surface with black ink. The ink marking could have degraded throughout the laser process and affected the focus of the laser, resulting in shallower etching in some regions. The trough seen next to the one-hour SIMS hole (Figure 21.b) is noticeably less noisy. This difference in signal quality is likely a result of different magnifications being used, with the LEXT having difficulties determining specific depths at lower magnifications. However, by taking the averages, the troughs can be approximated to be ~20 μm deep.

Due to the heavy presence of grains in the PCD samples, finding and determining the depth of the SIMS hole was not possible. Furthermore, as the BDSCD sample broke during removal from the SIMS, subsequent depth analysis was not possible. To then determine the etching rate, an average was taken for the rates observed on the two remaining samples (graphitised SCD and BDSCD_2). As seen in Figure 21.b and .c, the SIMS analysis has etched a depth of 2.4 and 4.1 μm for a one- and two-hour run. This constitutes an average etching rate of 2.2 μm/hour or 0.62 nm/s, a large increase from the calibrated value of 0.28 nm/s in 2014.

6.4 Laser Raman spectroscopy

(Laser) Raman spectroscopy is a technique frequently used to determine vibrational frequencies of molecules. In Raman spectroscopy, a monochromatic laser is focused using a microscope onto the sample surface. The laser excites electrons within the material, leading to inelastic scattering of photons. The photons are detected and measured using a charge-coupled device. With this, Raman spectroscopy can distinguish between diamond, amorphous carbon, and graphite, being able to analyse the carbon-phase composition of diamond samples.[118] Depending on the colour of the laser used, Raman results and intensities can vary heavily. When analysing diamond samples, green and blue lasers are shown to exhibit a distinct diamond peak at ~1332 cm^{-1}. Meanwhile, when using a red laser, a dominant luminescence peak at ~2270 cm^{-1} is observed alongside the diamond peak. When looking at BDDs, green lasers are shown to obtain the highest peak intensities out of the three colours.[119]

A Renishaw RM 2000 confocal micro-Raman system was used for the Raman analysis done in this thesis (Figure 22). The instrument, made by Renishaw (Wotton-under-Edge, United Kingdom), can be found in the diamond lab and operates with a green (514 nm) Ar$^+$ laser as an excitation source. The Windows-based Raman Environment (WiRE 2.0) software was used to set up spectral acquisitions and produce the data. The data was subsequently processed using Microsoft Excel, with a baseline correction being applied.

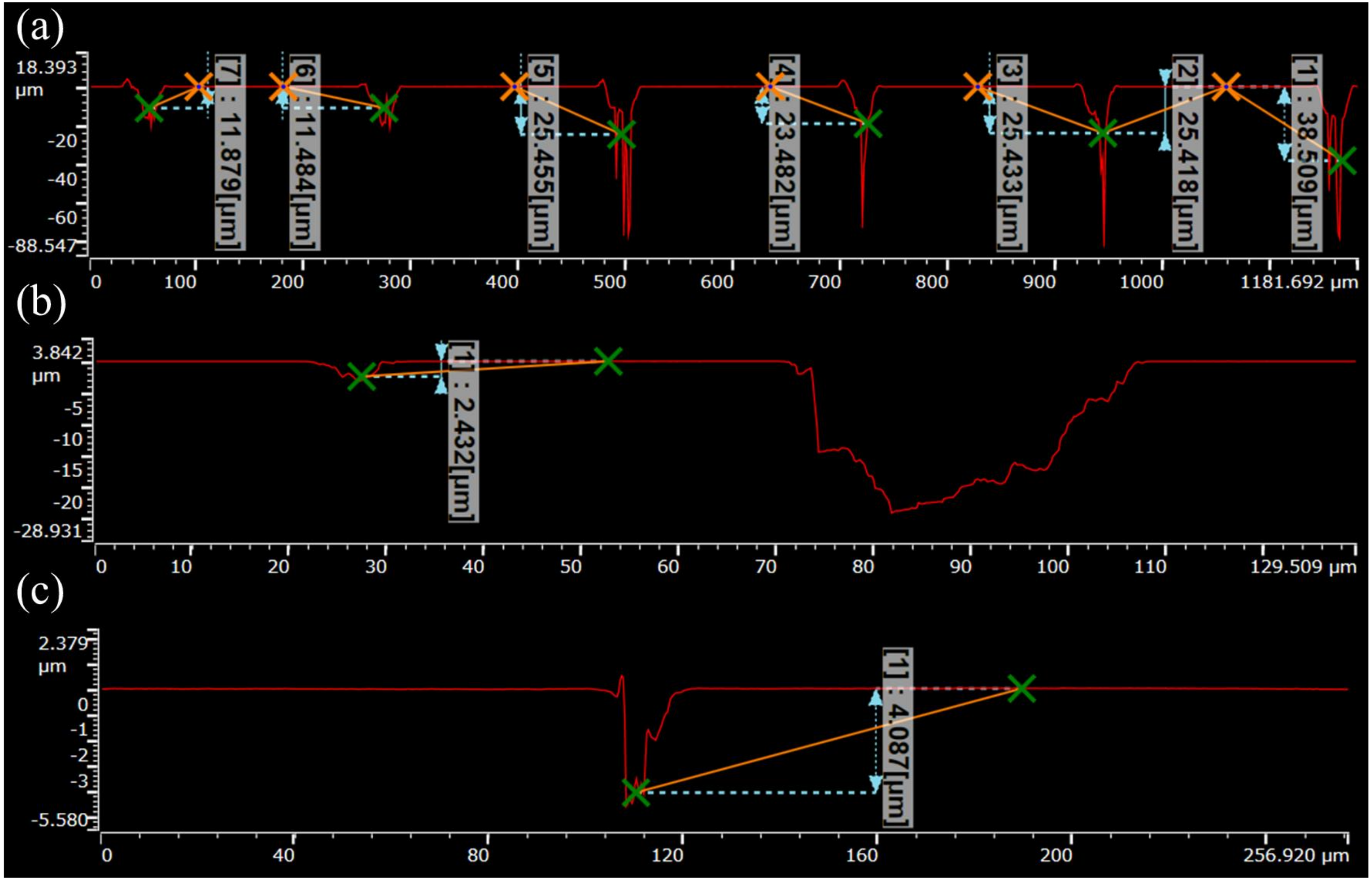

Figure 21. Depth analysis of (a) the etched regions of the graphitised sample at ×20, (b) etching from a one-hour SIMS depth profile on the graphitised sample at ×50, and (c) etching of a two-hour depth profile on the BDSCD_2 at ×100 magnification. Each depth measurement is taken as average (green cross) of the total etched regions and compared to either a single point (orange cross) or an average of the surface. The troughs in (a) are seen to change in depth throughout the sample. The etched trough of the graphitised sample is also visible on (b) but was not analysed.

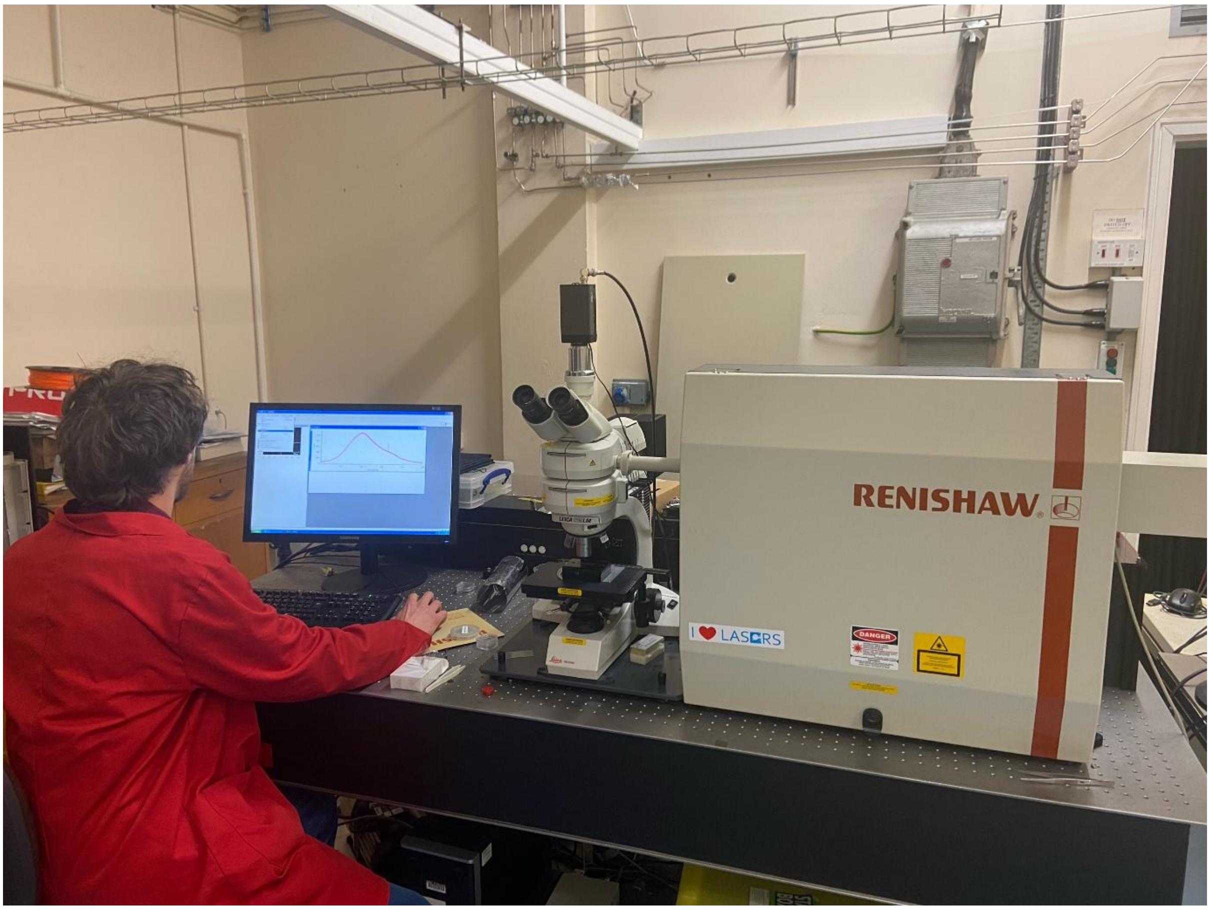

Figure 22. Image of the micro-Raman system found in the diamond lab. The sample is exposed to the laser through a ×50 lens on the optical microscope in the centre of the image. The microscope can also be used to observe the sample and determine the region being analysed.

Raman spectroscopy was performed on the three sample types to gain an understanding of their carbon phases. The analysis was repeated after the deuterium loading to determine any changes to the structure during the high-temperature loading process. The spectra for each sample type are presented in Figure 23. In addition to the analysis before and after the loading process, the etched regions of the graphitised sample were also analysed using the Raman spectrometer to gain insight into the extent of graphitisation resulting from the laser etching.

During the process, samples were placed onto the sample holder under a microscope at ×50 magnification, which was used to ensure the sample was properly focused and the laser was aimed at the correct region. Different areas of interest were also explored and are presented in each of the spectra for each sample type. Each spectrum consisted of five acquisitions, each with an exposure time of one second.

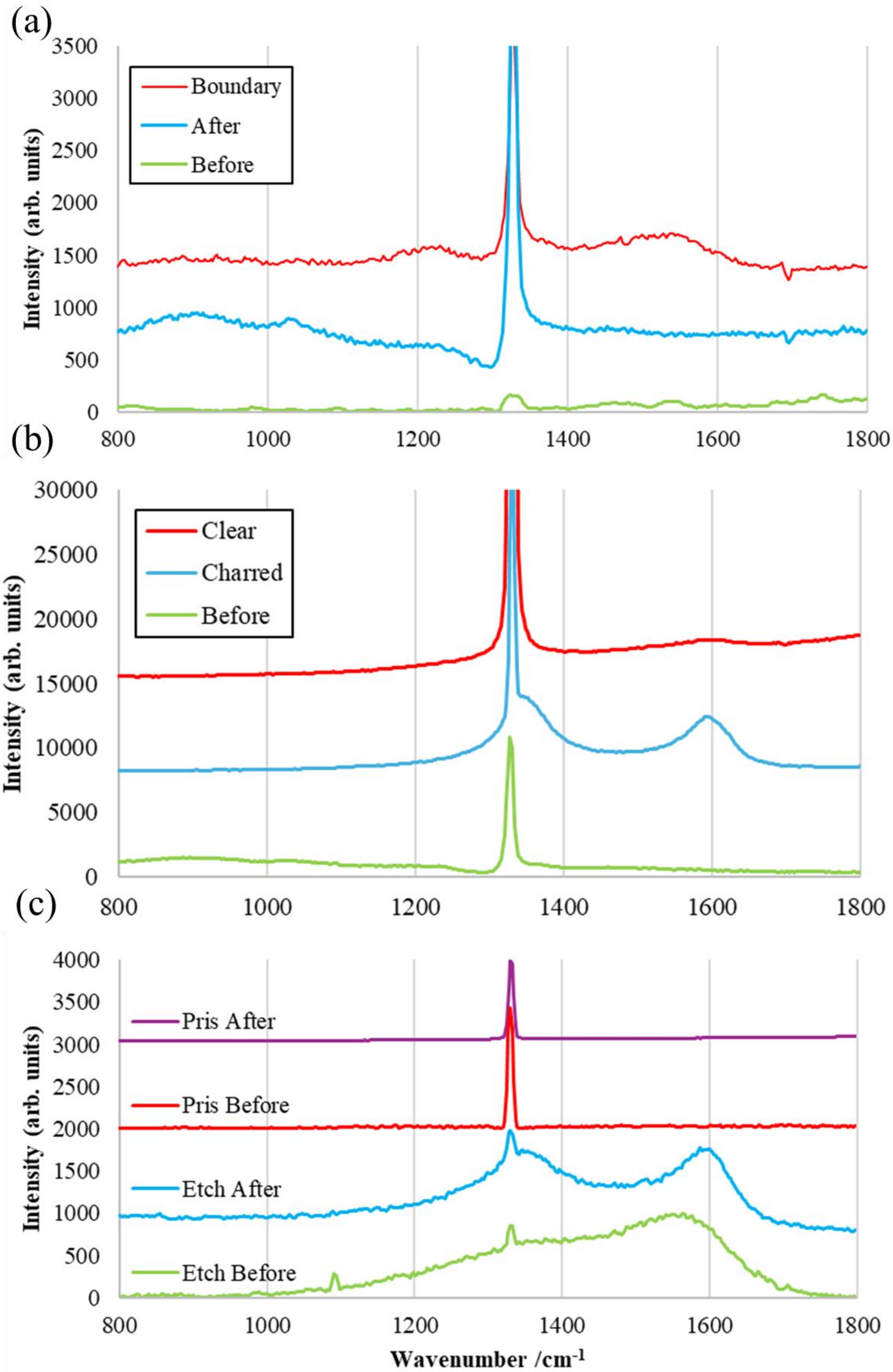

Figure 23. The Raman spectra of the (a) PCD, (b) BDSCD, and (c) graphitised SCD. For the PCD, spectra were taken before and after the loading process, focusing on large grains, with an additional spectrum also taken after in the grain boundary. The BDSCD had charred and clear regions after the loading process, both of which were compared to before the loading. The etched and pristine regions on the graphitised sample were also investigated before and after the loading process.

6.4.1 Deuterium loaded PCD

For the PCD sample, larger grains were targeted for analysis to reduce the number of defects at the exposure site. Raman spectra were obtained for the deuterium-loaded PCD sample before and after the loading process. An additional spectrum was taken at a grain boundary to establish and compare any differences against the grains.

When looking at the Raman spectrum for the PCD before deuterium loading (green, Figure 23.a), a diamond peak at 1332 cm^{-1} is observed weakly. The intensity for the whole spectrum is very low with a large rising background, which required heavy baseline correction to form a legible spectrum. As this was the first Raman analysis, and similar behaviour was unseen in subsequent peaks, the low intensity and quality were likely due to poor technique when focusing the laser. There is a very weak band observed at ~1550 cm^{-1}; this band is also weakly observed in the spectrum for the grain boundary (red) and could correspond to the graphitic 'G' band observed for sp^2 hybridised carbon.[120] The G band has previously been observed in microcrystalline diamond films, with larger bands consistent with poorer quality of the diamond.[118] This observation is in line with expectations, where grain boundaries introduce defects and are seen to exhibit graphite-like coordination, consisting of 80% threefold coordinated atoms.[121] This suggests that while the aim was to focus within a grain, a boundary could have been analysed instead. Moving onto the spectrum taken after the loading process (blue), apart from the 1332 cm^{-1} diamond peak, there is only a dip in the spectrum before the characteristic diamond peak. The lack of a band at 1200 cm^{-1}, which is commonly observed for heavily boron-doped diamonds, suggests the sample is lightly boron doped.[122, 123]

6.4.2 Deuterium loaded BDSCD

After deuterium loading, the sample has a clear change in colour, shifting from a dark-blue tone commonly observed for boron-doped diamonds to a more translucent centre with a darker charred edge (Figure 24). Due to the unexpected change, the carbon phases of the charred and clear region were analysed with Raman spectroscopy. The colour change is not purely aesthetic, demonstrating a clear difference in the Raman spectra taken (Figure 23.b) between the clear (red) and charred (blue) regions. In the clear region (red), the only distinct peak is the 1332 cm^{-1} peak, with a very slight, almost unnoticeable G band. Meanwhile, the charred region (blue) indicates that the sample has been graphitised with a prevalent G band and a new 'D' band at ~1400 cm^{-1}, corresponding to disordered graphite.[118, 120] This suggests that the edges, and the centre to a much lower extent, have been graphitised during the loading process. However, as the phenomenon is not observed in the PCD or the pristine regions of the graphitised SCD (Figure 23.a & 23.c), it is likely a result of the boron content of the SCD.

6.4.3 Graphitised SCD

As the graphitised sample had two separate regions, pristine and etched, both regions were analysed before and after the loading process, and the spectra are presented in Figure 23.c. When comparing the two regions before the loading, the laser etching is seen to damage the diamond, resulting in graphitisation. This is made evident by the broad D and G bands observed for the etched region (green), almost masking the 1332 cm^{-1} diamond peak, which is only faintly observable. A faint peak at ~1150 cm^{-1} is also observed in the spectrum and is suspected to stem from trans-polyacetylene (t-PA) segments.[124] These t-PA segments are commonly associated with nanocrystalline diamonds but have been observed in diamond samples that have been etched with O_2 plasma.[125, 126] The t-PA peak is not observed after the loading process (blue), possibly indicating that the process has degraded the t-PA, which is suspected to possess differing chemical reactivity than diamond due to its unique bonding.[127] Another reason behind the disappearance of the peak could be the variability of the defects throughout the diamond, where it is difficult to replicate results with such a specific technique as Raman spectroscopy.

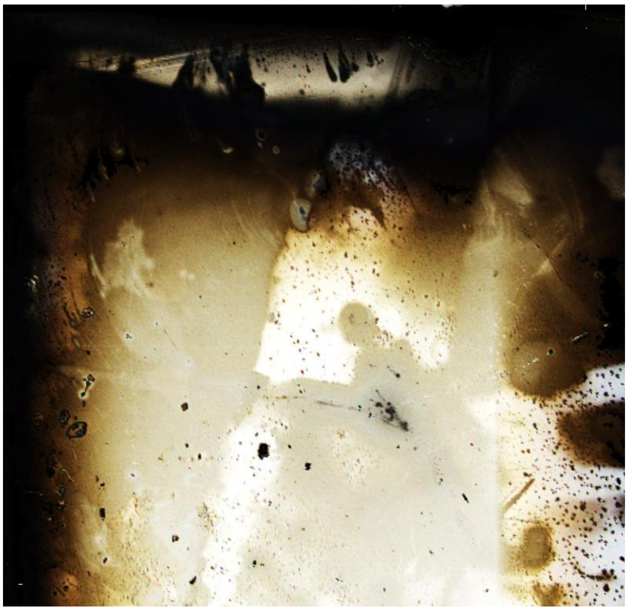

Figure 24. LEXT image of top half of the BDSCD sample after the deuterium loading, taken at ×10 magnification. The edges are clearly darker, exhibiting 'charring' of the surface, while the centre of the diamond is shown to be clearer.

6.5 Secondary Ion Mass Spectrometry

SIMS is a destructive process used to analyse the elemental or molecular composition and their spatial distribution in thin films. SIMS, as a technique, can characterise a broad range of elements with a high level of sensitivity. Time-of-flight (TOF) SIMS detection limits for hydrogen and deuterium in silicon were measured to be 3 x 10^{19} and 1.5 x 10^{18} atoms/$cm^{3,}$ respectively, highlighting a much higher sensitivity than other common analytical techniques.[128] SIMS involves the bombardment of the surface with a primary ion beam and accumulating the ejected secondary ions for mass spectrometry. While it is a destructive technique, SIMS can analyse samples very locally, being able to selectively bombard areas at the micrometre scale.

The SIMS analyses performed for this thesis were done using the SIMS instrument at the University of Bristol Interface Analysis Centre (Figure 25). After the loading process, samples were analysed using SIMS to measure the content of various elements in the diamond samples. For the SIMS process, a control sample for both SCD and PCD was used to compare and determine the effectiveness of the thermal loading process. Samples were loaded onto a stage and angled 45° to properly align the ion gun and detector. SIMS depth profiles were measured using a Ga^+ ion gun firing at 25 keV through a magnification of ×3000. A beam current of ~3.0 nA was measured using a Keithley (Cleveland, United States) model 6482 picoammeter with the beam in a Faraday cup. A "gating" facility was in place to reject secondary ions resulting from the sidewalls of the etched holes.

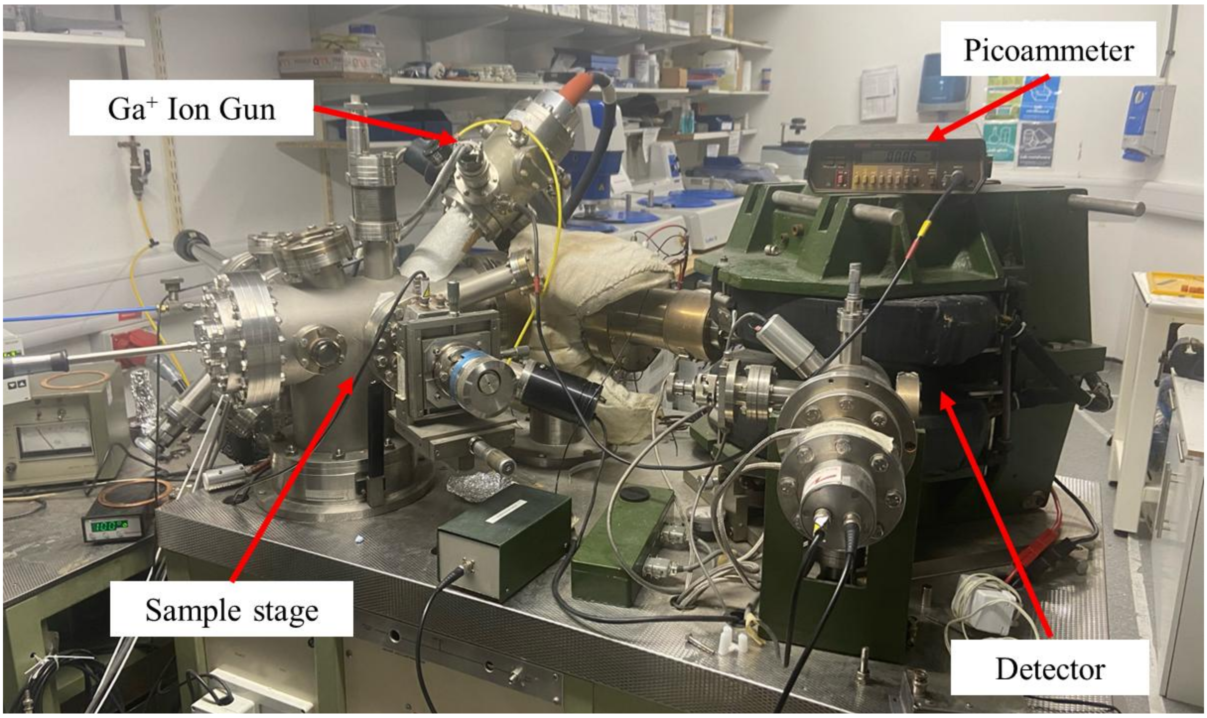

Figure 25. Annotated image of the SIMS instrument found in the Interface Analysis Centre at the University of Bristol. The system is constantly kept at UHV with samples being loaded into a separate vacuum chamber before being moved onto to the sample stage.

The specific SIMS parameters used for every sample are outlined in Table 4. Due to the age of the instrument and the power source, it was difficult to properly focus the detector, with some samples requiring higher ion amplification settings to gain a signal on the sample. As mentioned in section 6.3, post-SIMS 3D analysis of the SCD samples allowed the etching rate to be estimated. In 2014, the etching rate was assumed to be ~1.0 µm/hour (precisely being

Table 4. Summary of the SIMS parameters which were changed throughout the study. Dwell times remained constant for carbon (100 µs) as well as H, D, HD, D_2 (1000 µs).

Sample	Ion Amplification (amps)	Run Time (hours)	B Dwell Time (µs)	Si Dwell Time (µs)
BDPCD control	10^{-8}	1	1000	100
H-BDPCD	10^{-8}	1	1000	1000
SCD control	10^{-7}	1	100	100
D-SCD	10^{-8}	1	100	100
D-BDSCD	10^{-8}	1	100	100
D-BDSCD-2	10^{-7}	2	100	100
D-BDPCD-2	10^{-7}	1	100	100
BD-Frenkel	10^{-7}	5	100	100
i-Frenkel	10^{-7}	5	100	100

0.28 nm/s), however, the recent SIMS runs have demonstrated average etching rates of 2.2 μm/hour (Figure 21).

6.6 Thermal Desorption Spectra

TDS is another analytical technique that is valuable in its high sensitivity to quantify small amounts of hydrogen isotopes present in various materials. In principle, the technique is the inverse of the loading process employed in this thesis. In this method, samples are heated under ultra-high vacuum (UHV), leading to desorption of molecules incorporated within the lattice. These molecules are analysed by mass spectrometry, allowing for bulk concentrations of elements to be inferred. TDS offers an advantage over SIMS in that it can analyse the deuterium content across a whole sample rather than in specific localised areas. However, this could also be a disadvantage, where some samples would benefit from localised analysis (such as the graphitised SCD). Another advantage of TDS is that it offers information on the type of bonding, where the activation energy for desorption and coverage can be inferred from the temperature required for the constituent to diffuse out of the bulk.[129]

Therefore, to supplement the SIMS analysis, TDS was performed on one deuterium-loaded SCD to gain insight into how the deuterium was incorporated within the lattice. The TDS performed for this thesis was carried out by A. Zafra (Department of Engineering Science at the University of Oxford), using a Hidden Analytica Ltd. Type 640100 TPD workstation.[130] The TDS operates at UHV using a quadrupole mass spectrometer as the detector. The sample was placed on a hot plate that was heated up to 1000 °C from room temperature at a rate of 10 °C/min. Once 1000 °C was reached, the temperature was held for an hour. To protect the TDS instrument from contamination, an aluminium nitride layer was employed between the sample and the hot plate. The layer reduced the temperatures reached by the sample, requiring a temperature correction to be applied to the data. Temperature correction was determined by analysing argon desorption from a Si substrate.

Calibration factors for the TDS instrument were obtained using leak calibration tests for both H_2 and D_2, whereas the calibration factor of HD was taken as an average of the two values. To infer the deuterium content from the factors, the integral of the corrected counts must be multiplied with the calibration factors, giving the total number of deuterium atoms measured. To gain a concentration, the number of deuterium atoms must be divided by the area of the sample investigated.

7. Results & Discussion

7.1 Processing and presentation of the data

A large majority of the data processed and analysed was from SIMS. Initially, the SIMS instrument outputs elemental composition values as a percentage of the surface or maximum count observed. Due to this, the data must be converted into specific counts, which then have to be standardised as a ratio of the total number of carbon counts to account for the high sensitivity of the instrument (Figure 26). To make the graphs more legible and to account for extreme outliers, a rolling average of ten data points was taken. A rolling average was also used for the data received from the TDS.

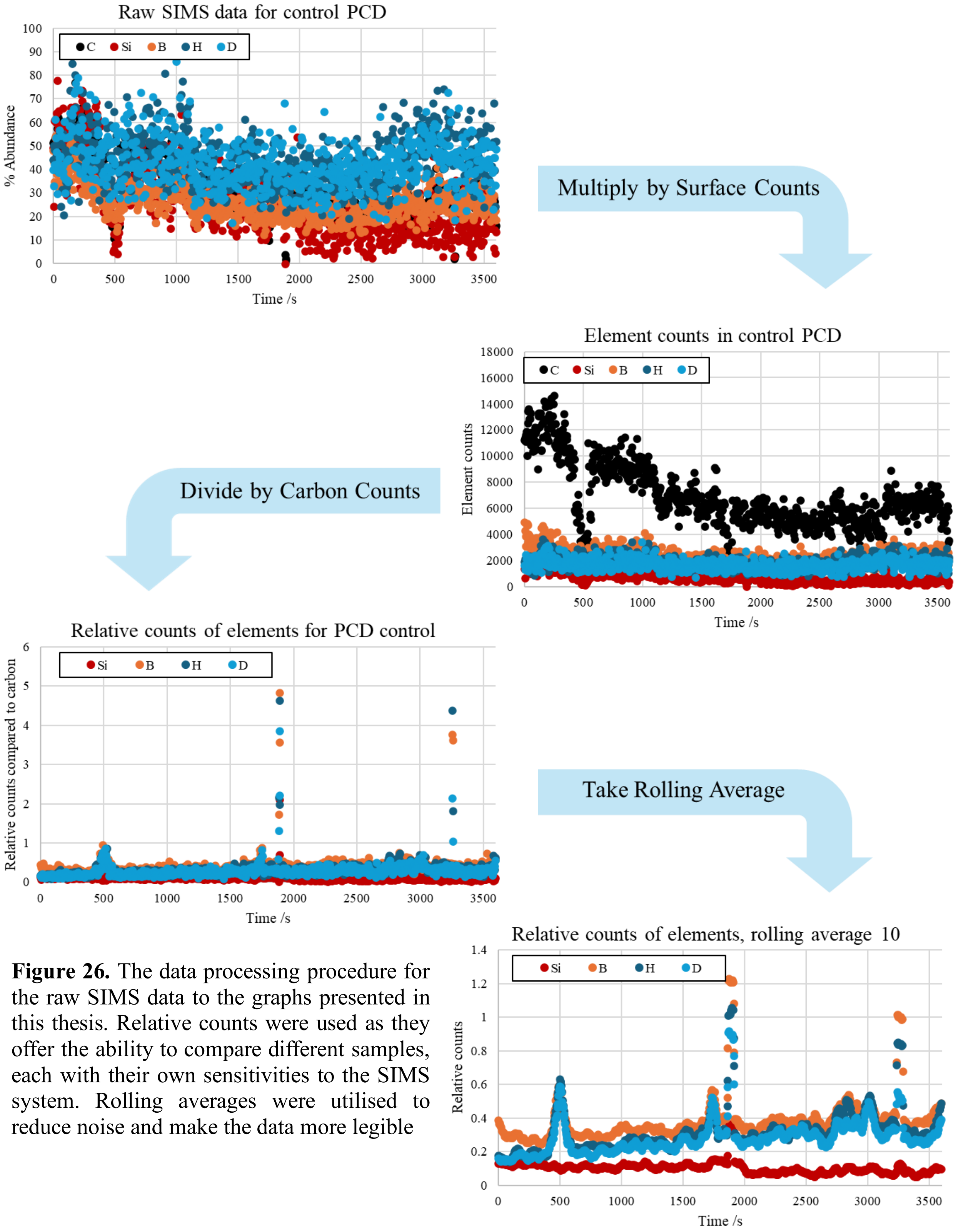

Figure 26. The data processing procedure for the raw SIMS data to the graphs presented in this thesis. Relative counts were used as they offer the ability to compare different samples, each with their own sensitivities to the SIMS system. Rolling averages were utilised to reduce noise and make the data more legible

7.2 Sample Weighing

To gain an initial estimate of the amount of hydrogen/deuterium loaded, samples were weighed before and after the loading process. Due to time constraints with the loading process and the availability of the SIMS instrument, the weighing was performed after the SIMS analysis. While SIMS is a destructive technique, the amount of material removed during the process was determined to be insignificant on a milligram scale. From LEXT imaging (Figure 21), the SIMS is shown to etch at a rate of ~2.2 µm/hour. If the SIMS is assumed to etch in a ~10 μm^3 cube (2.2^3), a large exaggeration, the etching process would remove 2.2 x 10^{11} diamond unit cells (with a cell taken to be 4.55 x $10^{-11} \mu m^3$ in size).[131] An individual diamond unit cell contains 18 carbon atoms, 14 of which are shared with its neighbours. If these shared atoms are considered distinct for each unit cell, the etched region would consist of ~4 x 10^{12} carbon atoms, weighing in at 7.8 x 10^{-11} grams, or 78 pg. Therefore, even when overestimating the number of carbon atoms and size of the area etched, the SIMS process should have a negligible impact on the weight of the samples.

With this in mind, the weight differences before and after the loading processes are listed in Table 4. The only sample which had a significant change in mass was the etched SCD, which decreased in mass by 0.09 mg. The decrease in mass is likely a result of the sample chipping at the edges near the etched digits. This chipping of the sample was observed when looking at the sample under the LEXT and is the likely culprit. For the two other measured samples, there was no significant change in mass, with both samples increasing in mass by 0.01 mg, which is within the error of the measuring instrument.

If the mass increases in Table. 5 are taken to be accurate, a change in mass of 0.01 mg would constitute 6 x 10^{18} hydrogen atoms or 3 x 10^{18} deuterium atoms. For a sample that is 6.8 mm by 3.3 mm in size (for the SCD sample), 3 x 10^{18} deuterium atoms reaching a maximum depth of ~10 µm (the expected maximum) would constitute a concentration of ~10^{22} atoms per cm^3(75000 ppm), an unprecedented amount. Due to this, it is very reasonable to assume that the change in mass is a result of the error associated with the instrument. Moreover, the calculation also demonstrates that to record the change in mass from deuterium implantation, a much more sensitive scale needs to be utilised, and thus, subsequent samples were not measured before or after the loading process. On the bright side, the fact that there is no negative change in mass in the BDSCD and PCD suggests that there is no significant etching of the samples during the loading process.

Table 5. Mass differences of weighed samples before and after the hydrogen and deuterium loading process. Masses were measured using a five-decimal gram weighing scale.

Sample	Weight before loading (mg)	Weight after loading (mg)	Difference (mg)
H-BDPCD	58.35	58.36	+ 0.01
D-BDSCD	18.38	18.39	+ 0.01
D-SCD	16.52	16.43	- 0.09

7.3 Control samples

To determine whether significant amounts of deuterium were implanted into the samples, SIMS was performed on two reference samples that had not been thermally loaded with either hydrogen or deuterium. SIMS for the BDPCD control was initially done for the hydrogen loading and thus did not measure counts for HD and D_2. Furthermore, the BDPCD control sample was done using an amplifier setting of 10^{-8} A, while the SCD control was done at 10^{-7} A. A subsequent analysis of the BDPCD control was to be done for the deuterium; however, due to limited timeframes between loading runs and loss of the initial deuterium loaded BDPCD, the sample was chosen to be loaded with deuterium instead.

When examining the trends in both the PCD and SCD control (Figure 27), it is evident that the sudden spikes, in the case of the PCD, are a result of the sudden drops in the carbon counts. The same can be said for the SCD, where the slow rise in relative counts over time is consistent with the decline in carbon counts. The SIMS depth profile for the BDPCD control (Figure 27.a) is as expected, with a high boron concentration followed by H and D (H_2), which are expected to incorporate into the sample during the deposition process. On the other hand, the results for the SCD control (done at 10^{-7} A) seem to suggest that the relative counts of boron almost equal that of hydrogen and deuterium (Figure 27.b). The pristine SCD sample is undoped and stated to have a boron concentration of <0.05 ppm ($<10^{16}$ atoms per cm^3).[116] But as the relative counts are similar, this also implies that very little hydrogen (H and H_2) is present in the SCD. This is unusual as the CVD-grown diamond is expected to contain hydrogen at a higher concentration than 0.05 ppm, suggesting that the SIMS instrument might have a difficult time detecting hydrogen at lower ion amplification settings.

When comparing the two controls, the relative counts should be unaffected by the difference in amplification. However, when looking at the results (Figure 27.c), this is not the case, and the relative counts observed for the higher amplification are significantly larger. Furthermore, the difference seems to be amplified for the lighter elements, where the higher amplification might be necessary to observe the counts in the first place. In the comparison, the Si counts seem to be somewhat close, being within an order of magnitude between both samples, especially towards the end of the analysis. On the other hand, there is a large difference between the relative H and D counts by an order of two magnitudes, further highlighting that the ion amplification might be necessary when dealing with light atoms.

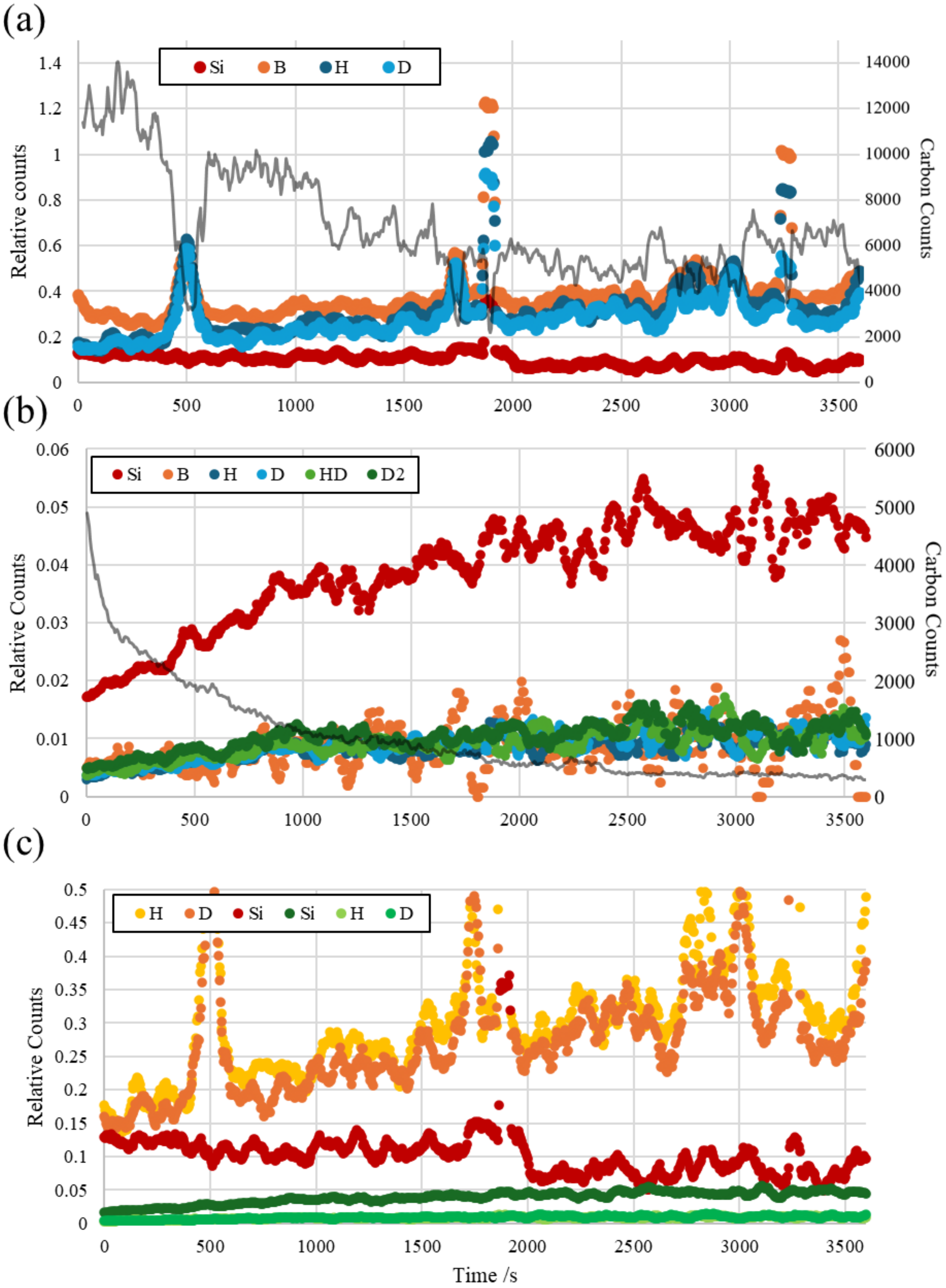

Figure 27. Processed SIMS results for the (a) BDPCD and the (b) SCD controls. Trends in the element counts can be related to changes in the carbon count (black). The two results are compared in (c) where the BDPCD (red, orange, yellow) is seen to have significantly larger relative counts than the SCD (green) control.

7.4 Hydrogen & Silicon BDPCD test

There was a concern that the high temperatures of the loading process could result in the etching of the quartz (SiO_2) tubing that could subsequently contaminate the diamond samples with silicon and oxygen. Therefore, to address and measure the extent of the contamination, Si^+ counts were measured in the SIMS analysis for the initial hydrogen loading test (O^- counts could not be measured as the SIMS analysis was run in positive ion mode). The relative element counts for the hydrogen-loaded PCD are compared to the control in Figure 28. For the loaded PCD, the SIMS instrument was knocked, resulting in the large spike in carbon counts seen at ~1400 seconds. After the spike, the raw data was noticeably noisier and non-carbon counts began to increase relative to the carbon. While the spike should not affect the relative counts, due to the source and nature of the increase, some uncertainty should be associated with conclusions drawn from data beyond ~1400 s.

Looking at the relative counts for the loaded PCD (Figure 28.b), Si is present in the sample. However, relative Si counts are relatively similar between the sample and the control, suggesting Si contamination to not be a large issue. Looking at the other elements (H, H_2, and B) in the loaded PCD (Figure 28.b), the trend in counts seem to follow each other closely. The correlation between the observed hydrogen and boron counts hints at boron possibly housing the implanted hydrogen, forming boron-hydrogen complexes within the diamond lattice. DFT calculations on boron-hydrogen complexes in diamond have found stable structures involving a single B impurity with up to four interstitial hydrogens.[132, 133]

On the other hand, the relative counts for the control PCD are as expected, with low concentrations of Si compared to hydrogen and boron. Similar to the loaded PCD, the hydrogen counts seem to correlate heavily with the boron counts. While there are spikes present in the relative counts, they are easily explained by the troughs observed in the carbon counts. Much more information can be inferred when comparing the two SIMS results.

Intriguingly, the relative boron counts are slightly higher in the loaded sample (Figure 28.c). The difference in relative boron counts only starts to widen after ~1400 s, the point at which the instrument was knocked, and data became unreliable. Due to this, it can be presumed that there is only a slight difference in boron counts between samples, likely resulting from miniscule differences in the manufacturing process.

When comparing the hydrogen counts (Figure 28.d), there does seem to be some increase in the loaded sample. However, it is important to note that the increase is consistent with the difference in relative boron counts, suggesting that the higher counts could be a result of the increased boron concentration rather than the loading process. Furthermore, as the differences are consistent between the B, H, and H_2 counts, it could result from the knocking of the instrument observed at ~1400 s. Due to these circumstances, the difference in hydrogen content between the two samples cannot be taken as significant enough to determine whether the loading process was successful.

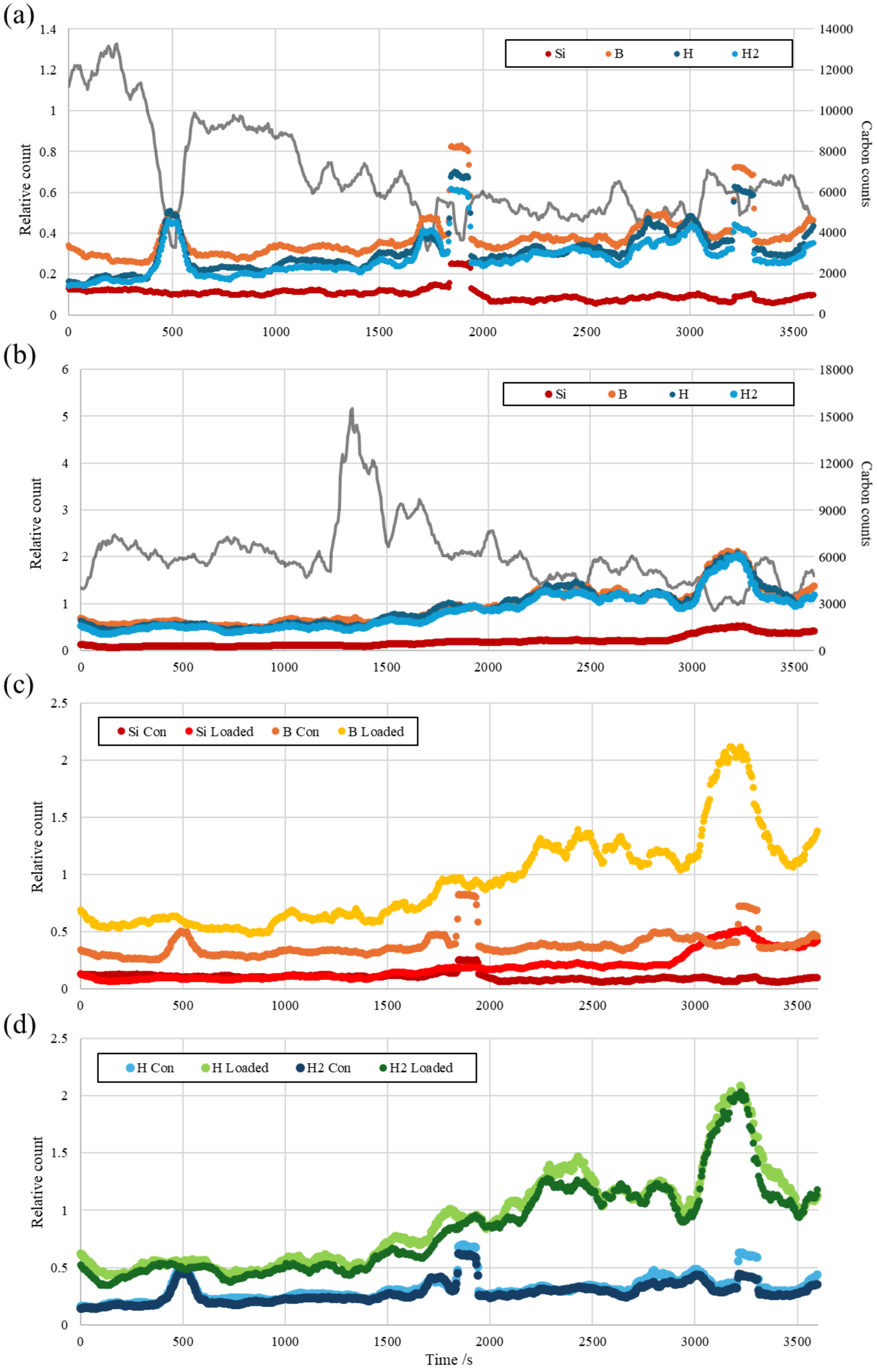

Figure 28. The SIMS data for (a) the BDPCD control (Con), (b) the hydrogen loaded BDPCD (Loaded), (c) Silicon and Boron, and (d) Hydrogen relative counts for the two samples. Note that the relative Si counts for the loaded PCD had a higher dwell time and thus was scaled down by an order of magnitude.

7.5 Deuterium loading on SCD, BDSCD, and control SCD

After the initial hydrogen test, one of each sample type (graphitised SCD, BDSCD, and BDPCD) was loaded with deuterium. The samples, along with a SCD control, were then analysed using the SIMS instrument to determine the extent of deuterium implantation, and the results are presented below in Figure 29. Unfortunately, the deuterium-loaded PCD was dropped into the vacuum chamber of the SIMS (Figure 30), being unretrievable for the near future. Due to this, only the SIMS results for the graphitised and BD SCD are compared against the control. HD and D_2 counts were chosen for the comparison as unlike D, which can be mistaken for H_2, the species only exist as a result of deuterium in the diamond. When taking the graph at face value, a significant difference between the HD and D_2 counts of the loaded samples against the SCD control is observed (Figure 29.a).

The HD and D_2 counts seem to be the closest to the control for the pristine SCD, while the BDSCD and the graphitised SCD are seen to contain significantly higher amounts of deuterium. These results are as expected, where the undoped and relatively defect-free SCD will hold the least amount of deuterium. While it is difficult to distinguish on the graph, the relative deuterium counts observed for the pristine SCD are still 2-3 times higher than the control, demonstrating that the thermal loading could still be working, just to a smaller extent. Meanwhile, both the etched and the BD SCD have deuterium counts which are an order of magnitude higher than the control. This data seems to support the hypothesis that an increase in the number of defects will increase the amount of deuterium retained in the sample.

When comparing the etched and the BD SCD, the etched sample is shown to retain a lot more deuterium at deeper levels. The increase in counts over time is observed for all element counts as it is likely due to the decrease in carbon counts over time observed in previous SIMS runs. While this decrease in carbon counts is also observed for the BD SCD, the effect on the relative count is not as prominent. A possible reason behind the difference in relative count is that the boron layer was very thin and only accounted for a small part of the depth profile, and thus, the doping will not be able to affect the deuterium retention at deeper levels. Another factor which could have affected the retention of the BDSCD would be the loss of boron throughout the loading process. It was noticed that the sample had lost some of its colour after being in the tube furnace, suggesting that boron had been diffused out of the diamond. This could negatively affect the deuterium retention due to the 'healing' of the lattice at high temperatures, a phenomenon observed for boron-doped diamonds.[134, 135]

Due to the uncertainty involved in the comparison between the loaded samples and the SCD control, the samples were also compared against the SIMS analysis of the PCD control that was done using an amplifier setting of 10^{-8} amps. As the SIMS analysis for the PCD control did not involve HD or D_2, the samples had to be compared with their relative H and D (H_2) counts (Figure 29.b). In the comparison, there seems to be no significant difference between the counts observed for the pristine SCD and the control. Meanwhile, the etched SCD has the highest observed counts, being more than an order of magnitude larger than the control. The BD SCD is also observed to have higher counts than the control, although not to the same extent as the etched regions, indicating there is higher retention in the etched SCD.

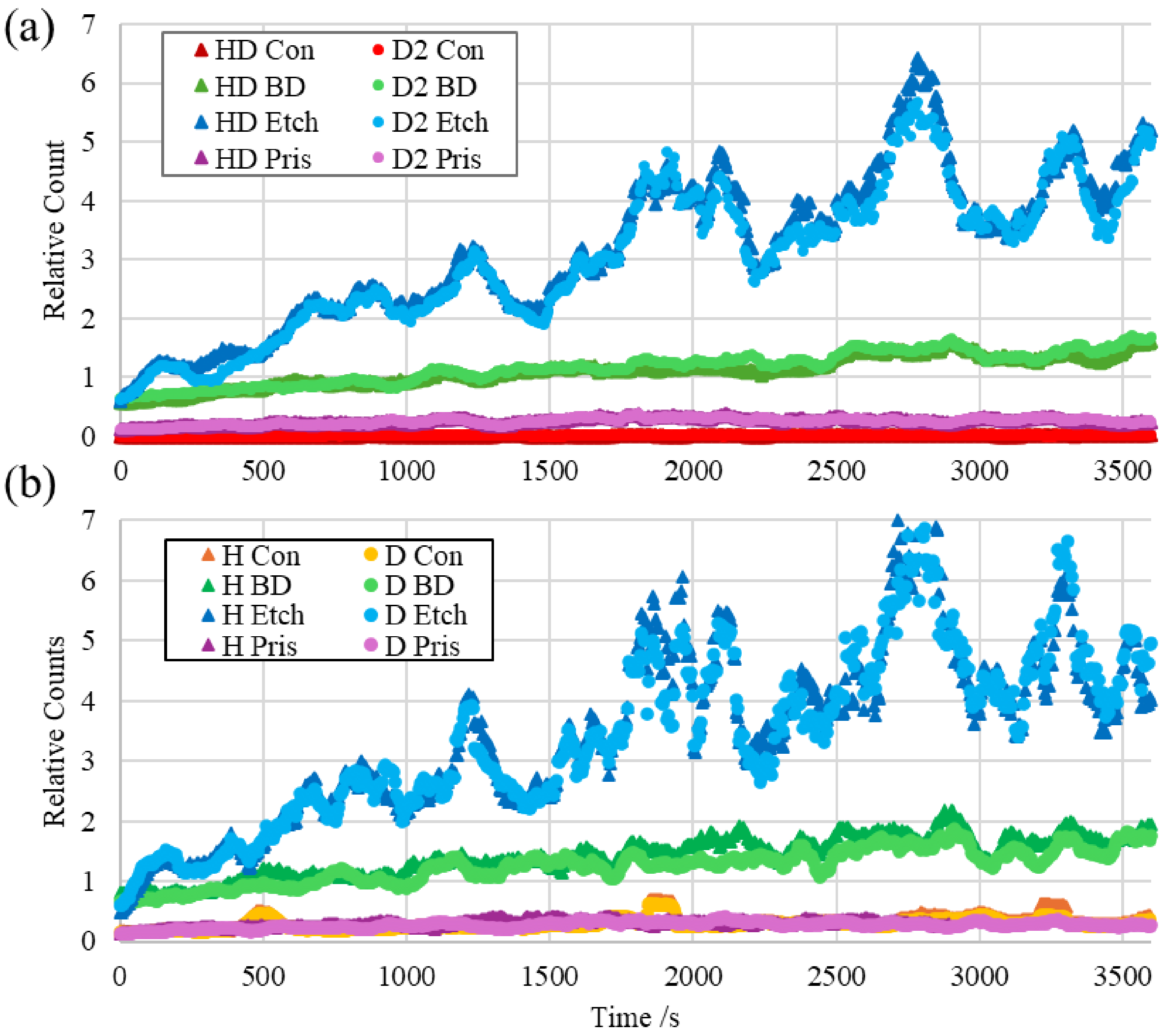

Figure 29. Comparisons of the hydrogen and deuterium counts of the BDSCD (BD) and both the pristine (Pris) and the etched (Etch) regions of the graphitised SCD samples against (a) the SCD control and (b) the PCD control (Con).

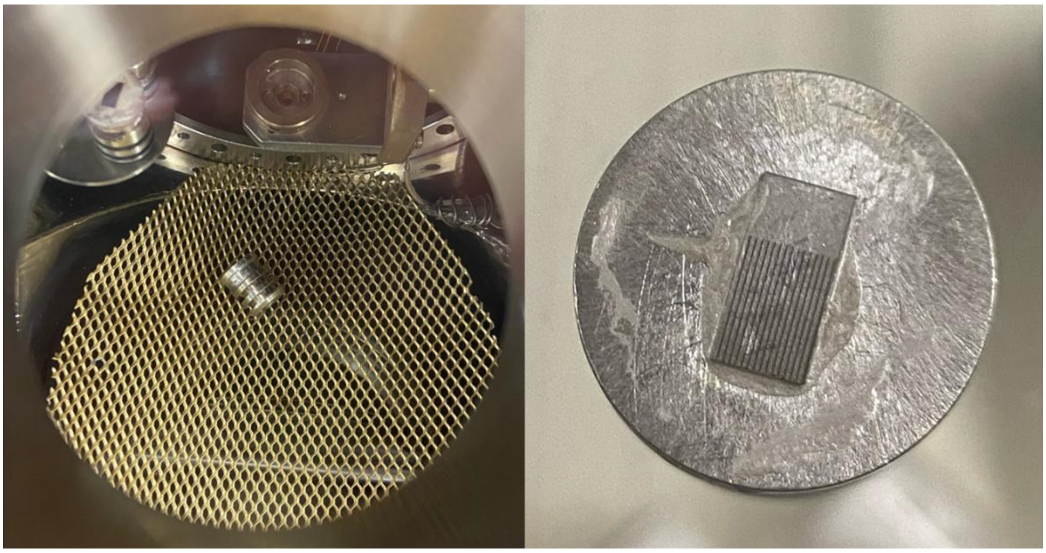

Figure 30. Images of the dropped BDPCD inside the SIMS UHV chamber (left) and the graphitised SCD sample on the mounting stage used to hold and manoeuvrer the samples within the chambers (right).

7.6 Deuterium loading 2 on BDSCD and BDPCD

To further understand the difference that ion amplification has on the hydrogen and deuterium counts, a second BDSCD and BDPCD were loaded with deuterium. These samples were subsequently analysed by SIMS using an ion amplifier setting of 10^{-7}. The results are presented in Figure 31, along with a comparison to the SCD control (also run at 10^{-7}). In the spectra for the BDPCD-2 (Figure 31.a), HD and D were omitted from the spectra to increase legibility and as qualitative conclusions of hydrogen and deuterium content can already be drawn from H and D_2. The BDPCD-2 sample is shown to contain a large amount of Si, a recurring observation for all samples. Moreover, the sample is expected to contain hydrogen from the deposition process; thus, the fact that similar counts of H and D_2 are observed suggests deuterium is present in the sample at a sufficient level. Both B and Si had shorter dwell times, and thus their counts are expected to be an order of magnitude larger than presented in the Figure 31, suggesting that both Si and B are present at much higher concentrations than the hydrogen isotopes.

The relative counts for the BDSCD-2 are slightly lower than those for the BDPCD-2. However, the counts are less noisy, possibly indicating that a better signal was obtained. Within the spectra, the boron layer is easily recognisable and seems to only be ~0.3 μm thick. The sample is shown to contain a similar amount of silicon as the BDPCD-2 but with lower hydrogen and deuterium counts. Yet again, the hydrogen and deuterium counts are similar, suggesting deuterium is present in the sample, at least to the same extent as the hydrogen. The D (H_2) and D_2 counts are slightly higher than the H and HD counts, suggesting that hydrogen and deuterium might prefer to incorporate as a molecule within the lattice. This phenomenon is also observed by TDS analysis of deuterium-implanted diamonds performed by Kimura *et al.* where almost all of the implanted deuterium desorbed as the D_2 molecule.[136]

When both samples are compared against the control (Figure 31.c), there seems to be no significant difference in the deuterium content of the BDSCD-2. Meanwhile, relative HD and D_2 counts for the BDPCD-2 are roughly double those for the control. This suggests that while deuterium counts are observed, the counts could be a result of background noise similar to dark current for photosensitive devices. Also, when compared to the results from the previous section, the differences in counts between the loaded samples and the control appear to be much smaller, supporting the idea that a higher ion amplification might be needed. When looking at the heavier elements (Figure 31.d), the control sample seems to contain more Si than the two loading samples, reiterating the lack of silicon contamination from the loading process. The BDPCD-2 seems to contain Si at similar levels to the control, which drops off due to a decrease in carbon counts. On the contrary, there is a stark difference in the observed boron counts. This is as expected, as the pristine SCD is undoped while the two loaded samples are boron doped. The grown boron layer is prominent for the BDSCD-2, after which the counts decrease to the same level as the PCD. This behaviour is strange as the boron count is expected to decrease to the baseline (SCD control) but instead seems to equal the BDPCD-2. This could be a result of boron diffusing throughout the lattice when exposed to the high temperatures of the loading process and could suggest that the BDPCD-2 is very lightly boron doped.

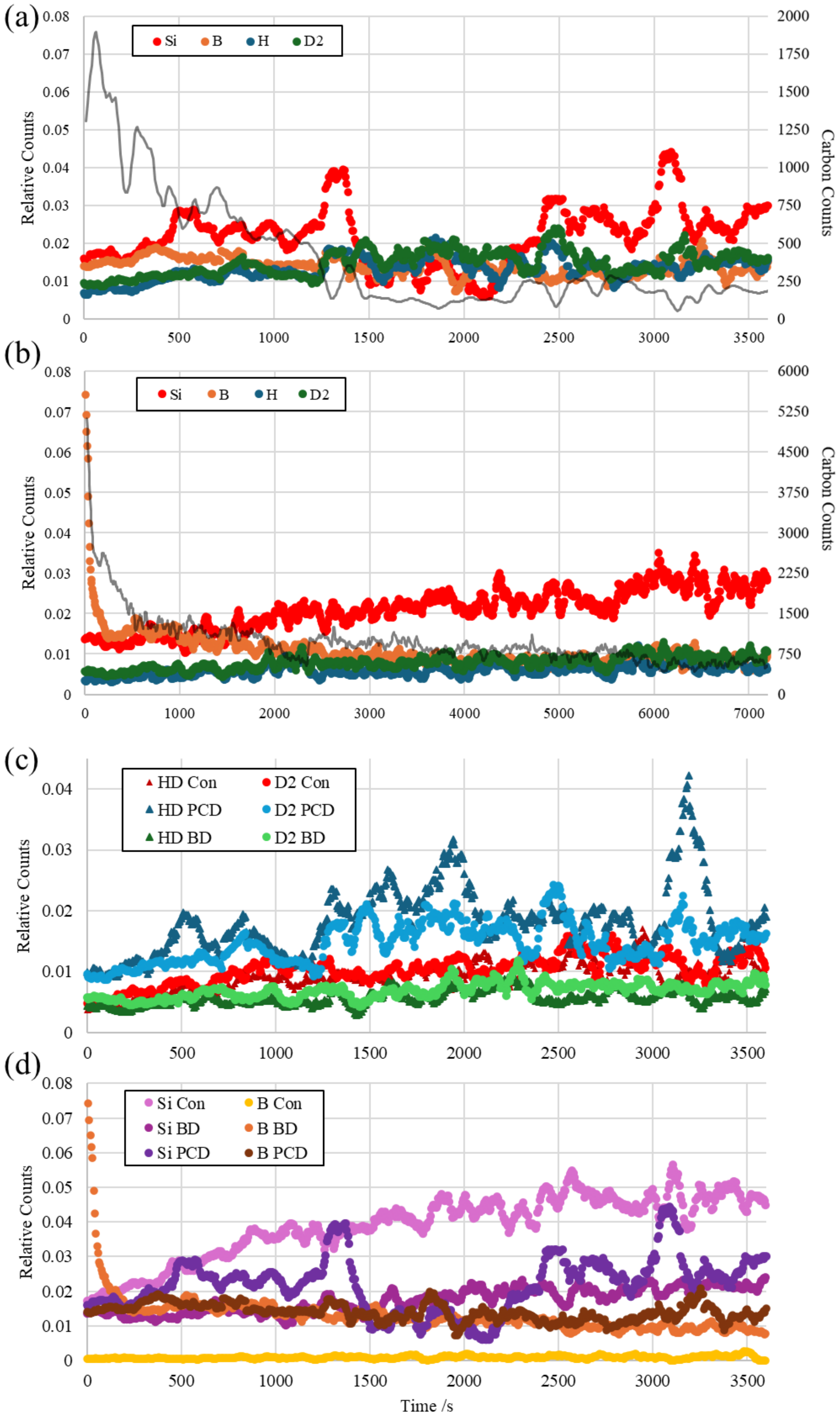

Figure 31. SIMS results for the deuterium loaded (a) BDPCD-2 (BD) and (b) BDPCD-2 (PCD). The carbon counts (black) are also presented in (a) and (b). Comparison of (c) the HD and D_2, and (d) the Si and B counts are also presented. Note that the BDSCD-2 had a longer analysis time (2 hours) which is not presented in the comparisons.

7.7 Deuterium loading on Oxford samples

As discussed previously, two SCD samples (one intrinsic and one BD) were laser etched to induce Frenkel defects under the surface. The samples were loaded with deuterium separately to ensure no boron contamination of the intrinsic sample. As these defects were induced 5 µm below the surface, the samples were analysed by SIMS for five hours to ensure the affected area was reached. For both samples, SIMS was performed using an ion amplification of 10^{-7} and are presented in Figure 32 below.

One concern was that the thermal loading process would not be able to incorporate deuterium 5 µm into the lattice. However, Cherniak *et al.* have observed deuterium to diffuse through PCD at a rate of ~80 nm^2/s at 900 ºC. Therefore, deuterium diffusing through a PCD at 1000 ºC could reach a maximum depth of >10 µm in four hours.[137] The study utilised PCDs, while the two Frenkel samples are SCD, which has been shown to have differing diffusion characteristics. Simulated diffusion in diamonds performed by Pittard *et al.* has shown deuterium to diffuse at faster rates in PCDs than SCDs, preferentially traveling through grain boundaries.[138] However, the SIMS results still suggest that the diffusion rate was significant enough to observe deuterium at depths >5 µm.

The intrinsic sample (I-Frenkel) exhibits unusually high relative counts for both Si and H at the start of the analysis, possibly indicating a high level of contamination towards the surface. Otherwise, the relative counts are observed to be very similar to previous samples, with high Si counts accompanied by H, D, HD, and D_2 counts being roughly an order of magnitude smaller. As expected for an intrinsic sample, the boron counts are negligible and could be used as a baseline. When compared to the relative boron count baseline, the results indicate that hydrogen and deuterium are present, however, no large change in relative counts can be seen at ~8000 s (5 µm depth). Additionally, the relative H counts are noticeably higher than the other three species (D, HD, and D_2), suggesting that more hydrogen is present. This difference between hydrogen and deuterium is not observed in other samples and could suggest that i-Frenkel performed poorly in terms of deuterium retention as is expected for an intrinsic sample.

For the boron doped sample (BD-Frenkel), the thermal loading process seemed to heal the graphitised markings on the sample, making it difficult to verify whether the defect induced regions were analysed by the SIMS. Nevertheless, the results are very intriguing as there is a spike in counts observed at around 10000 s, which corresponds to an etching depth of ~6 µm. The spike is somewhat in line with the depth of the defects situated 5 µm into the sample. However, as it is observed for all element counts and coincides with a sudden drop in carbon counts, the spike could be due to a fault in the electronics similar to the one observed for the hydrogen-loaded BDPCD in Figure 28. Furthermore, as a similar phenomenon is not observed for I-Frenkel, the source of the increased counts is likely coincidental. Similar to BDSCD-2, the boron layer is prominent and is calculated to be ~0.6 µm thick, being twice as large as the BDSCD-2. The D (H_2) relative count is significantly larger than H, HD, and D_2, suggesting a lot of hydrogen, and possibly deuterium, is present in the sample. However, the disparity in counts between D (H_2) and other deuterium species (HD and D_2) suggests that BD-Frenkel also performed poorly in retaining deuterium.

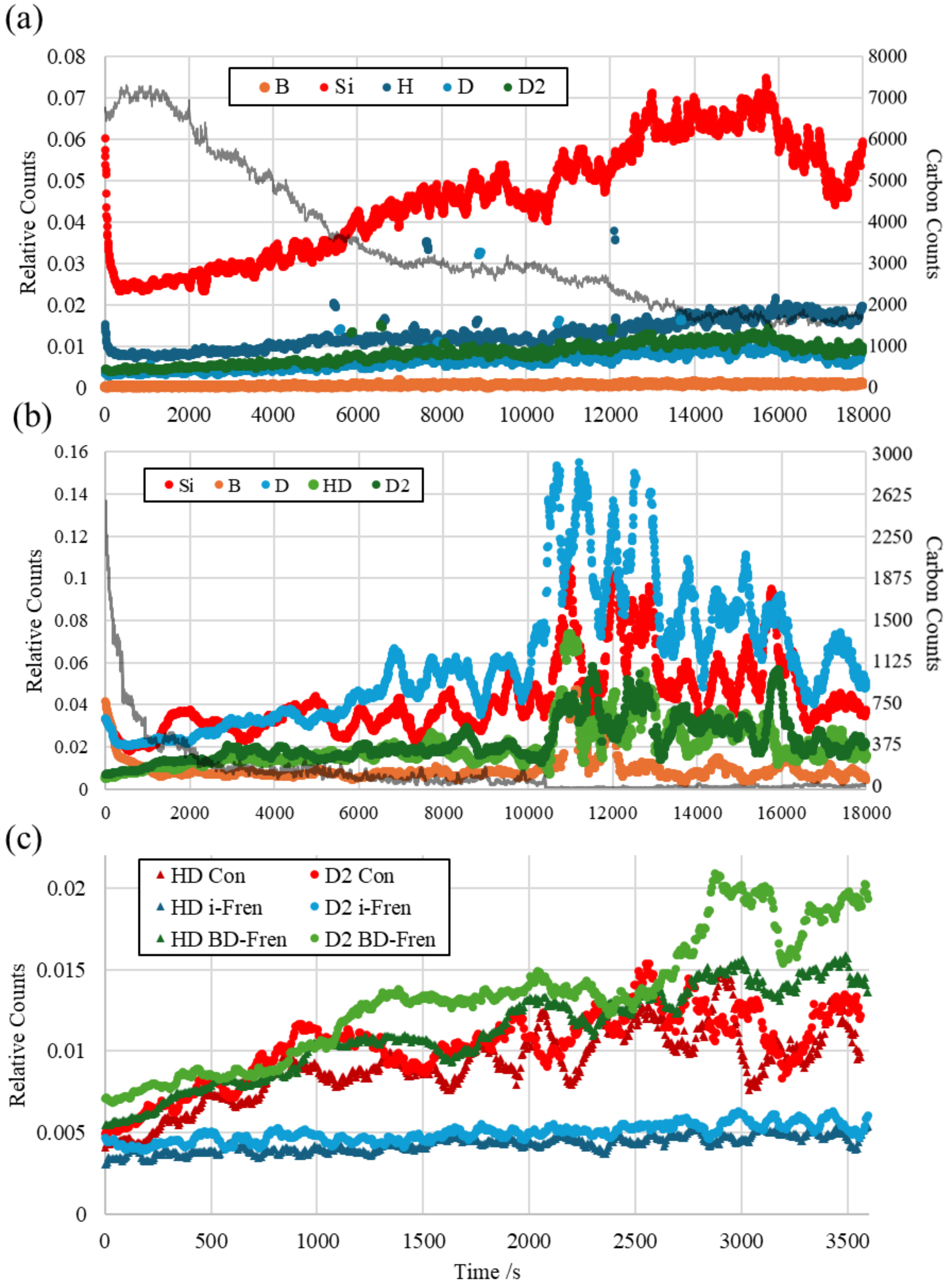

Figure 32. The SIMS results for (a) the i-Frenkel and (b) the BD-Frenkel samples. Their respective HD and D_2 are compared against the SCD control in (c). The HD and H relative counts were removed from (a) and (b) respectively to make the figures more legible.

7.8 TDS on BDSCD

The results of the TDS are presented in Figure 33 below. When looking at the HD and D_2 spectra, the samples do contain deuterium, being in line with the conclusions drawn from the SIMS results. When using the calibration factors, the total deuterium count measured by the TDS comes to ~3 x 10^{15} atoms, corresponding to a concentration of 1.4 x 10^{16} atoms/cm^2. TDS performed by Pittard *et al.* report deuterium concentrations for an reference PCD sample to be 3.31 x 10^{14} atoms/cm^2.[111] In the same paper, ion implantation with deuterium energies up to 1 keV are shown to implant deuterium at a concentration of ~6 x 10^{15} atoms/cm^2. This suggests that thermally loading samples with deuterium may result in greater retention than low energy ion implantation. This also goes against the results from the SIMS analysis, which suggests that the BDSCD-2 sample had relative deuterium counts similar to the control, which is expected to contain no deuterium.

For both the HD and the D_2 spectra, there seem to be two distinct peaks, a smaller peak at around 650 °C and a larger peak at around 867 °C, the highest temperature reached by the sample. The first smaller peak is also observed by Pittard *et al.* in their D_2 spectra (within 500-800 °C) and is suggested to belong to binding sites within the grain. This was further supported by the lack of the peak in the H_2 spectra, as the inter-grain binding sites would likely be inaccessible to hydrogen bound in the diamond.[15] Kimura *et al.* suggest the smaller peak occurs at such an energy as it originates from the detrapping of deuterium from a sp^3 C-D bond, a bond which has been shown to occur when diamond is irradiated with deuterium.[136, 139]

Meanwhile, the significant number of counts observed at the peak temperature (867 °C) suggests deuterium might still be trapped in the sample. This larger peak is observed by Pittard *et al.* and is proposed to occur from incorporation in grain boundaries, explaining why it is accessible to hydrogen and also observed in the H_2 spectra (Figure 33.b). However, the fact that the D_2 and the HD peak do not reach a stable plateau suggests that there is no constant outgassing of deuterium after the maximum temperature was met. This could be due to two reasons, one being that all the deuterium present in the diamond is being diffused out during the TDS, and thus, the deuterium counts start to decrease over time. This option is unlikely as the number of observed counts seems to decrease immediately upon reaching the maximum temperature. On the other hand, the thermally loaded deuterium could have found stable binding sites within the diamond that require higher temperatures to be released from. This is highly probable as the sample did not reach the same temperature as the one it was loaded at.

Kimura *et al.* suggested that deuterium counts observed from >850 °C are a result of bubbles present in the diamond, which they concluded by analysing the full width half maximum of their peaks. Due to the aluminium nitride coating limiting the maximum temperature, the second peak cannot be analysed fully, and similar conclusions cannot be reached. However, what can be concluded from the TDS is that the thermal loading was successful and seems to incorporate diamonds into some stable binding site.

The implications of this are that thermal loading seems to incorporate deuterium into stable binding sites rather than being diffused throughout the bulk. When under high temperature conditions (~1000 ºC), the deuterium atoms seem to find these stable sites to incorporate themselves in. For future work, it would be interesting to determine at what loading temperatures this binding occurs at and through TDS at higher temperatures, it would be useful to quantify the amount of deuterium present at this theorised binding site.

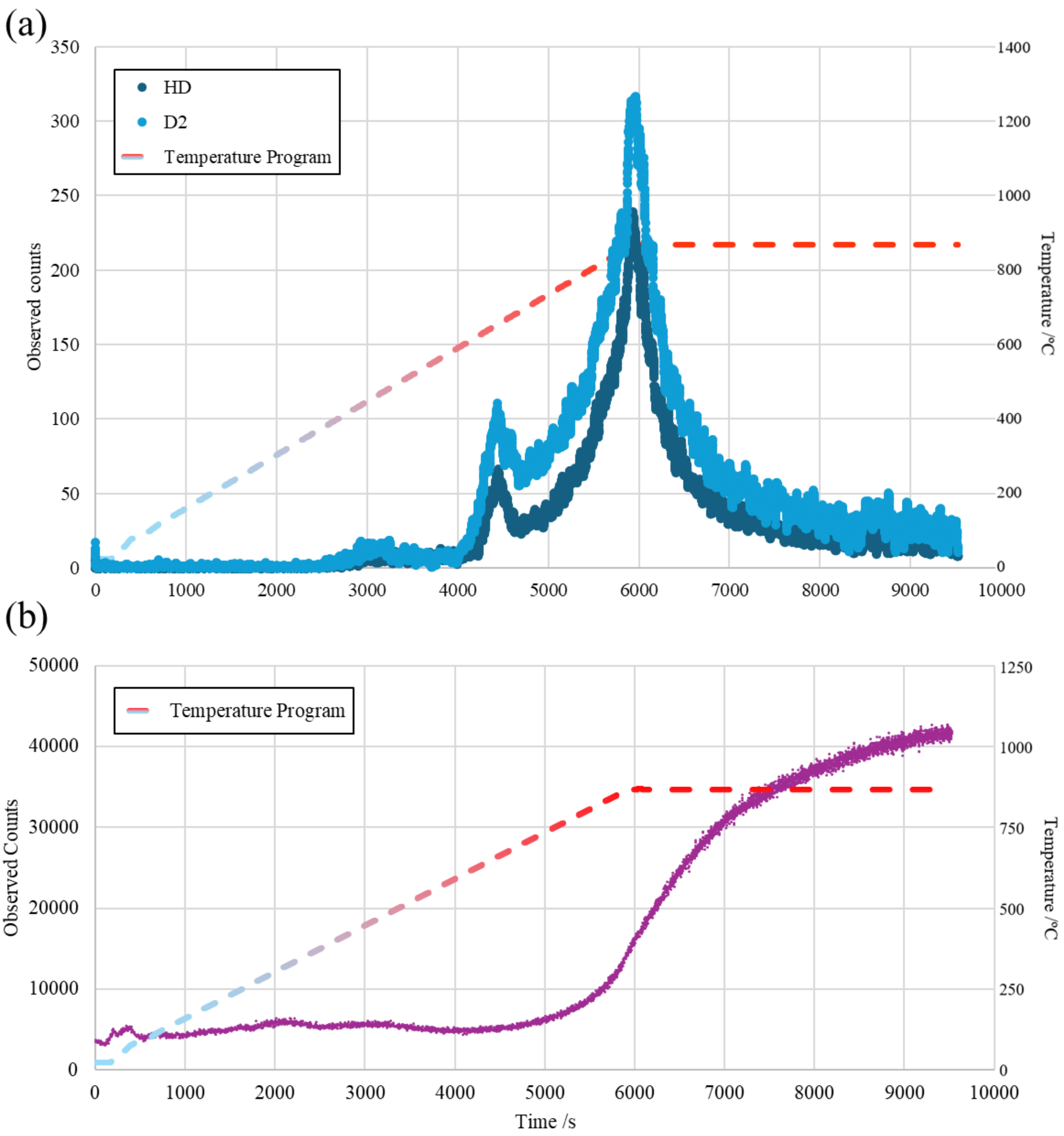

Figure 33. BDSCD-2 TDS results for (a) HD and D_2 counts and (b) H_2 counts. While the instrument reached a maximum temperature of 1000 °C, the aluminium nitride layer limited the temperature reached by the sample, which had to be estimated separately. The temperature program presented in the figure accounts for this and thus displays the temperature reached by the sample.

7.9 SIMS analysis of Boron doping

Although SIMS is often referred to as a qualitative technique, prior calibration of a known element composition can allow the technique to quantitatively measure concentrations. As it is quite difficult to implant a known amount of hydrogen or deuterium into a material, there is no [H] or [D] calibration for the SIMS instrument used. However, the SIMS instrument has been previously calibrated for boron concentrations using diamond samples that have been implanted with known quantities of B^+ ions:

$$Boron\ concentration\ [B]\ in\ atoms\ cm^{-3} = 1.8\ \times 10^{22} \times \left(\frac{B^+}{C^+}\right) \tag{1}$$

By applying the relative boron counts observed for the analysed samples into Equation 1, the boron concentration of the diamonds can be calculated. The comparison of the results with the expected boron concentrations of the samples can be found in Table 6.

Table 6. The average boron concentration calculated from SIMS depth profiling of the samples, compared to expected concentration values adapted from Ref. 117. Note that for some of the samples, (BDSCD-2 and BD-Frenkel) averages were only taken for the counts observed in the boron layer.

Sample	Average Boron concentration (atoms / cm^3)	Expected Boron concentration (atoms / cm^3)
BDPCD control*	6.11×10^{20}	2-6 × 10^{20}
H-BDPCD*	1.24×10^{21}	2-6 × 10^{20}
D-BDPCD-2	2.50×10^{20}	2-6 × 10^{20}
BDSCD*	3.78×10^{21}	~10^{22}
BDSCD-2	5.41×10^{20}	~10^{22}
BD-Frenkel	5.07×10^{20}	~10^{22}
Pristine SCD*	6.84×10^{21}	<10^{16}
Graphitised SCD*	7.65×10^{21}	<10^{16}

*Samples were run with a higher ion amplification setting of 10^{-8} A

When comparing the calculated concentrations with the expected, the average values for the BDPCD control seem to be in line with the expected values, being within the 2-6 × 10^{20} range reported by Element Six.[116] On the other hand, the [B] for the hydrogen-loaded BDPCD is almost double the upper limit. This large range in relative boron counts between seemingly similar samples is likely a result of the ion amplification. This is evident when looking at the calculated [B] for the undoped SCD, where both the pristine and graphitised regions are seen to contain a large amount of boron. While some boron could originate from contamination, the order of magnitude observed is highly unlikely, suggesting that the ion amplification is impacting the number of counts observed. This is also evidenced when comparing the BDSCD samples, which were all grown using the same MWCVD conditions. The two BDSCD samples (BDSCD-2 and BD-Frenkel), which were analysed with an amplification setting of 10^{-7} A, showed very similar concentrations, while the remaining BDSCD sample had a calculated [B] which was an order of magnitude larger. Further suggesting the inaccuracies involved at higher ion amplifications, especially for heavier elements.

To supplement the data in Table 7 and to evaluate the accuracy of the SIMS calibration, future work could encompass Raman spectroscopy to approximate the boron concentration of the diamond samples.[140]

8. Conclusions and Future Work

This thesis aimed to determine the feasibility of thermal deuterium loading in diamonds. Various types of diamonds were also investigated to evaluate the effect of defects and doping on the total amount of deuterium retained. When looking at the data, exposing diamonds to a high-temperature deuterium atmosphere seems to incorporate the gas into the diamond lattice. This is especially evident in the TDS results, where the BDSCD-2 sample was shown to contain a deuterium concentration of 1.4×10^{16} atoms/cm^2, being within the same order of magnitude as previous deuterium loading experiments done using ion implantation.[111, 136, 141]

While the thermal deuterium loading process is shown to incorporate deuterium into the diamonds, it is difficult to determine to what extent and depth each sample has been implanted with deuterium. Due to the age of the SIMS instrument, there is difficulty in distinguishing between elements with a lighter mass (H, D, HD, and D_2). The instrument also has a hard time detecting the lighter ions, possibly requiring a higher ion amplification than for heavier ions. However, as demonstrated by the calculated boron concentrations, there are also uncertainties observed for higher ion amplification settings.

Still, many samples have been observed to have relative deuterium counts larger than the two controls, highlighting that deuterium does incorporate into the lattice. There are some trends in the data which seem to support the conclusion that more deuterium is retained in areas with a higher number of defects. This is seen in the first set of deuterium loading runs (Figure 29), where the pristine SCD is shown to contain much less HD and D_2 than its boron-doped counterpart, which subsequently has less deuterium than the graphitised regions of the SCD. The trend is also noticed in the second set of samples (Figure 31.c), where the BDPCD, which contains many grain boundaries to house deuterium, is observed to have higher relative HD and D_2 counts than the BDSCD and the SCD control.

It was difficult to determine whether the induced defects in the i- and BD-Frenkel samples had an influence on the amount of deuterium retained (Figure 32). The results seem to indicate that for i-Frenkel, there was no noticeable change in relative counts, with the amount observed being lower than in the SCD control. On the other hand, there was a sudden increase in peaks observed for BD-Frenkel at ~6 μm deep. While the increase coincides with a decrease in carbon counts, there is a possibility that the sudden change in counts (both for carbon and deuterium) could be due to a change in the lattice structure. Therefore, a conclusion on the effect of Frenkel defects on deuterium retention cannot be made, and further investigation is required, possibly using a SIMS instrument with a more sensitive detector such as a quadrupole mass spectrometer.

Meanwhile, the TDS results demonstrate that the implanted deuterium occupies a stable binding site within the lattice, requiring high temperatures to diffuse out. Solid state computational modelling could be utilised to determine how the deuterium occupies said binding site(s). Future work could also involve loading the diamonds with deuterium at a lower temperature, investigating whether the implantation temperature has an impact on how the deuterium incorporates into the lattice. Additionally, higher temperature TDS would allow for the true amount of deuterium present in the sample to be calculated, giving insight into the effectiveness of thermal deuterium loading.

In the context of nuclear batteries, the experiments performed in this thesis show promise towards diamonds loaded with tritium. For the thermal loading of tritium, the results of this thesis suggest that a poly-crystalline diamond will offer the highest deuterium retention. This conclusion is in line with the literature, which suggests these boundaries comprise various sites for interstitial atoms to occupy.[87] With the tritium loading process, the main difficulty will lie in configuring a system that can handle and prevent tritium leakages. However, if such a system is implemented, the future fabrication of tritium-powered diamond batteries seems promising.

9. References

1. V. Bormashov, S. Troschiev, A. Volkov, S. Tarelkin, E. Korostylev, A. Golovanov, M. Kuznetsov, D. Teteruk, N. Kornilov, S. Terentiev, S. Buga and V. Blank, *physica status solidi (a)*, 2015, **212**, 2539-2547.
2. J. E. Field, *Properties of Natural and Synthetic Diamond*, Elsevier Science, 1992.
3. A. Mauger and C. M. Julien, *Ionics*, **23**, 2017.
4. K. Miyoshi, *Solid Lubrication Fundamentals and Applications*, CRC Press, 2019.
5. M. A. White, S. Kahwaji, V. L. S. Freitas, R. Siewert, J. A. Weatherby, M. D. M. C. Ribeiro da Silva, S. P. Verevkin, E. R. Johnson and J. W. Zwanziger, *Angewandte Chemie International Edition*, 2021, **60**, 1546-1549.
6. S. S. Dossa, I. Ponomarev, B. N. Feigelson, M. Hainke, C. Kranert, J. Friedrich and J. J. Derby, *Journal of Crystal Growth*, 2023, **609**, 127150.
7. I. Kiflawi, H. Kanda and S. C. Lawson, *Diamond and Related Materials*, 2002, **11**, 204-211.
8. F. D. Rossini and R. S. Jessup, *Journal of research of the National Bureau of Standards*, 1938, **21**, 491.
9. F. P. Bundy, W. A. Bassett, M. S. Weathers, R. J. Hemley, H. U. Mao and A. F. Goncharov, *Carbon*, 1996, **34**, 141-153.
10. M. Kamo, Y. Sato, S. Matsumoto and N. Setaka, *Journal of Crystal Growth*, 1983, **62**, 642-644.
11. P. W. May, *Philosophical Transactions of the Royal Society of London. Series A: Mathematical, Physical and Engineering Sciences*, 2000, **358**, 473 - 495.
12. M. N. R. Ashfold, P. W. May, J. R. Petherbridge, K. N. Rosser, J. A. Smith, Y. A. Mankelevich and N. V. Suetin, *Physical Chemistry Chemical Physics*, 2001, **3**, 3471-3485.
13. P. K. Bachmann, H.-J. Hagemann, H. Lade, D. Leers, F. Picht, D. U. Wiechert and H. Wilson, *MRS Online Proceedings Library*, 1994, **339**, 267-277.
14. J. R. Petherbridge, P. W. May and M. N. R. Ashfold, *Journal of Applied Physics*, 2001, **89**, 5219-5223.
15. J. P. Goss, R. Jones, M. I. Heggie, C. P. Ewels, P. R. Briddon and S. Öberg, *Physical Review B*, 2002, **65**, 115207.
16. K. Kobashi, in *Diamond Films*, ed. K. Kobashi, Elsevier Science Ltd, Oxford, 2005, pp. 25-27.
17. S. Matsumoto, Y. Sato, M. Kamo and N. Setaka, *Japanese Journal of Applied Physics*, 1982, **21**, L183.
18. T. Teraji, T. Yamamoto, K. Watanabe, Y. Koide, J. Isoya, S. Onoda, T. Ohshima, L. J. Rogers, F. Jelezko, P. Neumann, J. Wrachtrup and S. Koizumi, *physica status solidi (a)*, 2015, **212**, 2365-2384.
19. F. Silva, K. Hassouni, X. Bonnin and A. Gicquel, *Journal of Physics: Condensed Matter*, 2009, **21**, 364202.
20. Y. Ren, X. Li, W. Lv, H. Dong, Q. Cheng, F. Yue, N. Wöhrl, J. C. Mendes, X. Yang and Z. Li, *Journal of Materials Science: Materials in Electronics*, 2024, **35**, 525.
21. L. Cheng, S. Zhu, X. Ouyang and W. Zheng, *Diamond and Related Materials*, 2023, **132**, 109638.
22. C. J. H. Wort and R. S. Balmer, *Materials Today*, 2008, **11**, 22-28.
23. E. Johnson, 1958 IRE International Convention Record, IEEE, 1965.
24. R. W. Keyes, *Proceedings of the IEEE*, 1972, **60**, 225-225.
25. B. J. Baliga, *IEEE Electron Device Letters*, 1989, **10**, 455-457.

26. Y. Gong, W. Jia, B. Zhou, K. Zheng, D. Ma, Z. Li, J. Gao, Y. Ma, H. Hei, S. Yu, Y. Xue and Y. Wu, *Diamond and Related Materials*, 2023, **139**, 110377.
27. J. V. Macpherson, *Physical Chemistry Chemical Physics*, 2015, **17**, 2935-2949.
28. T. Yokoya, T. Nakamura, T. Matsushita, T. Muro, Y. Takano, M. Nagao, T. Takenouchi, H. Kawarada and T. Oguchi, *Nature*, 2005, **438**, 647-650.
29. P. W. May and R. Zulkharnay, *Phil Trans R Soc Lond A*, 2024.
30. R. Kalish, *Diamond and Related Materials*, 2001, **10**, 1749-1755.
31. S. Koizumi, M. Kamo, Y. Sato, S. Mita, A. Sawabe, A. Reznik, C. Uzan-Saguy and R. Kalish, *Diamond and Related Materials*, 1998, **7**, 540-544.
32. A. Traoré, Université de Grenoble, 2014.
33. R. Aly, R. Tarek, O. Ramadan, M. Khashan, A. Elmaghraby and P. Hossam, 2023.
34. S. V. Mukhamale, A. R. Chavan, R. M. Lokhande and P. P. Khirade, *Solar Energy*, 2020, **211**, 866-878.
35. G. S. Gildenblat, S. A. Grot, C. R. Wronski, A. R. Badzian, T. Badzian and R. Messier, *Applied Physics Letters*, 1988, **53**, 586-588.
36. A. Vescan, I. Daumiller, P. Gluche, W. Ebert and E. Kohn, *IEEE Electron Device Letters*, 1997, **18**.
37. K. Ueda, K. Kawamoto and H. Asano, *Diamond and Related Materials*, 2015, **57**, 28-31.
38. H. Umezawa, M. Nagase, Y. Kato and S.-i. Shikata, *Diamond and Related Materials*, 2012, **24**, 201-205.
39. J. E. Butler, M. W. Geis, K. E. Krohn, J. J. Lawless, S. Deneault, T. M. Lyszczarz, D. Flechtner and R. Wright, *Semiconductor Science and Technology*, 2003, **18**, S67.
40. N. Donato, N. Rouger, J. Pernot, G. Longobardi and F. Udrea, *Journal of Physics D: Applied Physics*, 2020, **53**, 093001.
41. Y. Intelligence, *Emerging Semiconductor Substrates 2023*, Yole Group, 2023.
42. 大熊ダイヤモンドデバイス、ダイヤモンド半導体工場建設に向け、PreAラウンドで約40億円を調達, https://prtimes.jp/main/html/rd/p/000000005.000120349.html, (accessed 30th November, 2024).
43. Diamfab Announces €8.7M Round of Funding from Asterion Ventures, Bpifrance and Fonds Régional Avenir Industrie Auvergne-Rhône-Alpes, https://diamfab.com/wp-content/uploads/2024/03/20240328-PR-Diamfab-announced-a-E8.7M-round-of-funding.pdf, (accessed November, 2024).
44. 'Diamond-age' of power generation as nuclear batteries developed, https://www.bristol.ac.uk/cabot/what-we-do/more-case-studies/2016/diamond-battery.html, (accessed November, 2024).
45. H. G. J. Moseley, *Proceedings of the Royal Society of London. Series A, Containing Papers of a Mathematical and Physical Character*, 1913, **88**, 471-476.
46. R. E. Faw and J. K. Shultis, in *Encyclopedia of Physical Science and Technology (Third Edition)*, ed. R. A. Meyers, Academic Press, New York, 2003, pp. 613-631.
47. G. R. Mackenzie, S. Kaluvan, P. G. Martin, C. Hutson, T. Connolley, M. Cattelan, H. Dominguez-Andrade, T. L. Martin, N. A. Fox and T. B. Scott, *Materials Today Energy*, 2021, **21**, 100688.
48. B. Liu, B. Dai, K. Liu, L. Yang, J. Zhao, G. Shu, Z. Lv, G. Gao, K. Yao, M. Bi, J. Xue, W. Wang, V. Ralchenko, J. Han and J. Zhu, *Diamond and Related Materials*, 2018, **87**, 35-42.
49. T. R. Alam, M. T. Tchouaso and M. A. Prelas, in *Photovoltaics for Space*, eds. S. G. Bailey, A. F. Hepp, D. C. Ferguson, R. P. Raffaelle and S. M. Durbin, Elsevier, 2023, pp. 293-345.

50. L. C. Olsen, *Energy Conversion*, 1973, **13**, 117-127.
51. L. C. Olsen, Lewis Research Center, NASA, 1993.
52. C. A. Klein, *Journal of Applied Physics*, 1968, **39**, 2029-2038.
53. Y. Liu, X. Tang, Z. Xu, L. Hong, P. Wang and D. Chen, *Science China Technological Sciences*, 2014, **57**, 14-18.
54. R. Zheng, J. Lu, Y. Wang, Z. Chen, X. Zhang, X. Li, L. Liang, L. Qin, Y. Zeng, Y. Chen and Y. Liu, *Applied Physics Letters*, 2022, **121**, 103902.
55. S. I. Maximenko, J. E. Moore, C. A. Affouda and P. P. Jenkins, *Scientific Reports*, 2019, **9**, 10892.
56. M. A. Prelas, C. L. Weaver, M. L. Watermann, E. D. Lukosi, R. J. Schott and D. A. Wisniewski, *Progress in Nuclear Energy*, 2014, **75**, 117-148.
57. M. Lu, G.-g. Zhang, K. Fu, G.-h. Yu, D. Su and J.-f. Hu, *Energy Conversion and Management*, 2011, **52**, 1955-1958.
58. Z. Cheng, X. Chen, H. San, Z. Feng and B. Liu, *Journal of Micromechanics and Microengineering*, 2012, **22**, 074011.
59. C. Zai-Jun, S. Hai-Sheng, C. Xu-Yuan, L. Bo and F. Zhi-Hong, *Chinese Physics Letters*, 2011, **28**, 078401.
60. C. Thomas, S. Portnoff and M. G. Spencer, *Applied Physics Letters*, 2016, **108**, 013505.
61. T. Shimaoka, H. Umezawa, K. Ichikawa, J. Pernot and S. Koizumi, *Applied Physics Letters*, 2020, **117**, 103902.
62. V. S. Bormashov, S. Y. Troschiev, S. A. Tarelkin, A. P. Volkov, D. V. Teteruk, A. V. Golovanov, M. S. Kuznetsov, N. V. Kornilov, S. A. Terentiev and V. D. Blank, *Diamond and Related Materials*, 2018, **84**, 41-47.
63. C. Delfaure, M. Pomorski, J. de Sanoit, P. Bergonzo and S. Saada, *Applied Physics Letters*, 2016, **108**, 252105.
64. M. Amirmazlaghani, A. Rajabi, Z. Pour-mohammadi and A. A. Sehat, *Superlattices and Microstructures*, 2020, **145**, 106602.
65. Technology NDB, https://ndb.technology/technology/, (accessed November, 2024).
66. Home | Arkenlight, https://www.arkenlight.co.uk, (accessed November, 2024).
67. S. Tarelkin, V. Bormashov, E. Korostylev, S. Troschiev, D. Teteruk, A. Golovanov, A. Volkov, N. Kornilov, M. Kuznetsov, D. Prikhodko and S. Buga, *physica status solidi (a)*, 2016, **213**, 2492-2497.
68. W. E. Matheson, in *Engineering in Medicine: Volume 1: Advances in Pacemaker Technology*, eds. M. Schaldach and S. Furman, Springer Berlin Heidelberg, Berlin, Heidelberg, 1975, pp. 401-424.
69. M. V. S. Chandrashekhar, C. I. Thomas, H. Li, M. G. Spencer and A. Lal, *Applied Physics Letters*, 2006, **88**, 033506.
70. Y. R. Uhm, B. G. Choi, J. B. Kim, D.-H. Jeong and K. J. Son, *Nuclear Engineering and Technology*, 2016, **48**, 773-777.
71. Y. Lei, Y. Yang, G. Li, Y. Liu, J. Xu, X. Xiong, S. Luo and T. Peng, *Applied Physics Letters*, 2020, **116**, 153901.
72. V. V. Bochkarev, G. B. Radzievsky, L. V. Timofeev and N. A. Demianov, *The International Journal of Applied Radiation and Isotopes*, 1972, **23**, 493-504.
73. J. Russo, M. Litz, W. Ray, G. M. Rosen, D. I. Bigio and R. Fazio, *Applied Radiation and Isotopes*, 2017, **125**, 66-73.
74. S.-K. Lee, S.-H. Son, K. Kim, J.-W. Park, H. Lim, J.-M. Lee and E.-S. Chung, *Applied Radiation and Isotopes*, 2009, **67**, 1234-1238.
75. NanoTritium™ Battery Technology, https://citylabs.net/technology-overview/, (accessed December, 2024).

76. H. Li, Y. Liu, R. Hu, Y. Yang, G. Wang, Z. Zhong and S. Luo, *Applied Radiation and Isotopes*, 2012, **70**, 2559-2563.
77. T. R. Alam, M. A. Pierson and M. A. Prelas, *Appl Radiat Isot*, 2017, **130**, 80-89.
78. C. Zhao, F. Liao, K. Liu and Y. Zhao, *Applied Physics Letters*, 2021, **119**, 153904.
79. V. I. Chepurnov, M. V. Dolgopolov, A. V. Gurskaya, A. A. Akimchenko, O. V. Kuznetsov, A. V. Radenko, V. V. Radenko and A. S. Mashnin, *Materials Science. Non-Equilibrium Phase Transformations.*, 2017, **3**, 119-120.
80. M.-S. Yim and F. Caron, *Progress in Nuclear Energy*, 2006, **48**, 2-36.
81. Y. Hwang, Y. H. Park, H. S. Kim, D. H. Kim, S. Ali, S. Sorcar, M. C. Flores, M. R. Hoffmann and S.-I. In, *Chemical Communications*, 2020, **56**, 7080-7083.
82. S. N. Bocharov, B. E. Burakov, A. I. Isakov, K. N. Orekhova, E. V. Dementeva, M. V. Zamoryanskaya, P. A. Dementev, B. Y. Ber, D. Y. Kasantsev, M. V. Tokarev and Y. Y. Petrov, *Diamond and Related Materials*, 2024, **141**, 110650.
83. UKAEA, Diamonds are forever? World-first carbon-14 diamond battery made, https://www.gov.uk/government/news/diamonds-are-forever-world-first-carbon-14-diamond-battery-made, (accessed December, 2024).
84. X. Li, J. Lu, Z. Chen, X. Liu, Y. Liu, Y. Zhang, Y. Zhang and F. Tian, *AIP Advances*, 2023, **13**, 115314.
85. G. S. Woods and A. T. Collins, *Journal of Physics and Chemistry of Solids*, 1983, **44**, 471-475.
86. J. P. F. Sellschop, C. C. P. Madiba and H. J. Annegarn, *Nuclear Instruments and Methods*, 1980, **168**, 529-534.
87. B. Dischler, C. Wild, W. Müller-Sebert and P. Koidl, *Physica B: Condensed Matter*, 1993, **185**, 217-221.
88. E. Holzschuh, W. Kündig, P. F. Meier, B. D. Patterson, J. P. F. Sellschop, M. C. Stemmet and H. Appel, *Physical Review A*, 1982, **25**, 1272-1286.
89. N. Sahoo, S. K. Mishra, K. C. Mishra, A. Coker, T. P. Das, C. K. Mitra, L. C. Snyder and A. Glodeanu, *Physical Review Letters*, 1983, **50**, 913-917.
90. J. Chevallier, A. Lusson, D. Ballutaud, B. Theys, F. Jomard, A. Deneuville, M. Bernard, E. Gheeraert and E. Bustarret, *Diamond and Related Materials*, 2001, **10**, 399-404.
91. C. C. P. Madiba, J. P. F. Sellschop, J. A. Van Wyk and H. J. Annegarn, *Nuclear Instruments and Methods in Physics Research Section B: Beam Interactions with Materials and Atoms*, 1988, **35**, 442-445.
92. W. M. Haynes, *CRC handbook of chemistry and physics*, CRC press, 2016.
93. Y. Konishi, I. Konishi, N. Sakauchi, S. Hayashi, A. Hirakimoto and J. Suzuki, *Nuclear Instruments and Methods in Physics Research Section B: Beam Interactions with Materials and Atoms*, 1996, **118**, 312-317.
94. M. S. Haque, H. A. Naseem, J. L. Shultz, W. D. Brown, S. Lal and S. Gangopadhyay, *Journal of Applied Physics*, 1998, **83**, 4421-4429.
95. C. J. Tang, A. J. Neves and M. C. Carmo, *Journal of Physics: Condensed Matter*, 2005, **17**, 1687.
96. S. Kaufman and W. F. Libby, *Physical Review*, 1954, **93**, 1337-1344.
97. *UNSCEAR 1977 Report*, United Nations Scientific Committee on the Effects of Atomic Radiation Vienna, Austria, 1997.
98. A. L. Carsten, in *Advances in Radiation Biology*, eds. J. T. Lett and H. Adler, Elsevier, 1979, vol. 8, pp. 419-458.
99. M. Ni, Y. Wang, B. Yuan, J. Jiang and Y. Wu, *Fusion Engineering and Design*, 2013, **88**, 2422-2426.

100. *UNSCEAR 2016 Report*, United Nations Scientific Committee on the Effects of Atomic Radiation, New York, 2016.
101. K. M. Song, S. H. Sohn, D. W. Kang and H. S. Chung, Korea, Republic of, 2005.
102. L. Stefan, N. Trantea, A. Bornea, M. Zamfirache, N. Bidica and I. Stefan, *Fusion Engineering and Design*, 2019, **146**, 1505-1509.
103. Hydrogen-3 Advanced Technology, https://ccfe.ukaea.uk/divisions/h3at/, (accessed December, 2024).
104. M. Kovari, M. Coleman, I. Cristescu and R. Smith, *Nuclear Fusion*, 2018, **58**, 026010.
105. A. Bergmaier, G. Dollinger, A. Aleksov, P. Gluche and E. Kohn, *Surface Science*, 2001, **481**, L433-L436.
106. G. Dollinger, A. Bergmaier, C. M. Frey, M. Roesler and H. Verhoeven, *Diamond and Related Materials*, 1995, **4**, 591-595.
107. N. Mizuochi, J. Isoya, J. Niitsuma, T. Sekiguchi, H. Watanabe, H. Kato, T. Makino, H. Okushi and S. Yamasaki, *Journal of Applied Physics*, 2007, **101**, 103501.
108. R. Bogdanowicz, M. Sobaszek, M. Sawczak, G. M. Grigorian, M. Ficek, P. Caban, A. Herman and A. Cenian, *Diamond and Related Materials*, 2019, **96**, 198-206.
109. R. D. Maclear, J. E. Butler, S. H. Connell, B. P. Doyle, I. Z. Machi, D. B. Rebuli, J. P. F. Sellschop and E. Sideras-Haddad, *Diamond and Related Materials*, 1999, **8**, 1615-1619.
110. P. K. Chatterjee, S. D. S. Malhi, M. deWit, H. Hosack, M. G. Harward and M. M. Moslehi, in *Reference Data for Engineers (Ninth Edition)*, eds. W. M. Middleton and M. E. Van Valkenburg, Newnes, Woburn, 2002, pp. 20-21-20-113.
111. J. A. Pittard, N. A. Fox, A. Hollingsworth, M. Y. Lavrentiev, A. Wohlers and Y. Zayachuk, *Fusion Engineering and Design*, 2023, **188**, 113403.
112. D. Ballutaud, F. Jomard, B. Theys, C. Mer, D. Tromson and P. Bergonzo, *Diamond and Related Materials*, 2001, **10**, 405-410.
113. C. Fernández-Lorenzo, D. Araújo, J. Martín, R. Alcántara, J. Navas, M. P. Villar, M. P. Alegre, P. N. Volpe, F. Omnès and E. Bustarret, *Diamond and Related Materials*, 2010, **19**, 904-907.
114. J. Chevallier, D. Ballutaud, B. Theys, F. Jomard, A. Deneuville, E. Gheeraert and F. Pruvost, *physica status solidi (a)*, 1999, **174**, 73-81.
115. D. Ballutaud, F. Jomard, J. Le Duigou, B. Theys, J. Chevallier, A. Deneuville and F. Pruvost, *Diamond and Related Materials*, 2000, **9**, 1171-1174.
116. Element Six E shop, https://e6cvd.com/uk/application/all.html, (accessed March, 2025).
117. T. Okuchi, H. Ohfuji, S. Odake, H. Kagi, S. Nagatomo, M. Sugata and H. Sumiya, *Applied Physics A*, 2009, **96**, 833-842.
118. J. Filik, *Spectroscopy Europe*, 2005, **17**.
119. R. Haubner and M. Rudigier, *Physics Procedia*, 2013, **46**, 71-78.
120. S. Prawer and R. J. Nemanich, *Philosophical Transactions of the Royal Society of London. Series A: Mathematical, Physical and Engineering Sciences*, 2004, **362**, 2537-2565.
121. P. Keblinski, D. Wolf, S. R. Phillpot and H. Gleiter, *Journal of Materials Research*, 1998, **13**, 2077-2100.
122. V. Mortet, A. Taylor, Z. Vlčková Živcová, D. Machon, O. Frank, P. Hubík, D. Tremouilles and L. Kavan, *Diamond and Related Materials*, 2018, **88**, 163-166.
123. P. Szirmai, T. Pichler, O. A. Williams, S. Mandal, C. Bäuerle and F. Simon, *physica status solidi (b)*, 2012, **249**, 2656-2659.
124. A. C. Ferrari and J. Robertson, *Physical Review B*, 2001, **63**, 121405.

125. X. Tan, Z. He, W. Li, Q. Yang, J. Wang, L. Cang, Y. Du and H. Qi, *ACS Omega*, 2024, **9**, 27492-27498.
126. Y. Zheng, H. Ye, J. Liu, J. Wei, L. Chen and C. Li, *Materials Letters*, 2019, **253**, 276-280.
127. L. Hu, Y. Guo, S. Du, S. Tian, J. Li and C. Gu, *Diamond and Related Materials*, 2021, **116**, 108415.
128. F. A. Stevie, C. Zhou, M. Hopstaken, M. Saccomanno, Z. Zhang and A. Turansky, *Journal of Vacuum Science & Technology B*, 2016, **34**, 03H103.
129. S. Ogura and K. Fukutani, in *Compendium of Surface and Interface Analysis*, ed. J. The Surface Science Society of, Springer Singapore, Singapore, 2018, pp. 719-724.
130. A. Baron-Wiechec, K. Heinola, J. Likonen, E. Alves, N. Catarino, J. P. Coad, V. Corregidor, I. Jepu, G. F. Matthews and A. Widdowson, *Fusion Engineering and Design*, 2018, **133**, 135-141.
131. D. Das, in *Carbon-Based Nanofillers and Their Rubber Nanocomposites*, eds. S. Yaragalla, R. Mishra, S. Thomas, N. Kalarikkal and H. J. Maria, Elsevier, 2019, pp. 123-181.
132. J. P. Goss, P. R. Briddon, S. J. Sque and R. Jones, *Physical Review B*, 2004, **69**, 165215.
133. E. B. Lombardi, *Diamond and Related Materials*, 2009, **18**, 835-838.
134. F. Agulló-Rueda, M. D. Ynsa, N. Gordillo, A. Maira, D. Moreno-Cerrada and M. A. Ramos, *Diamond and Related Materials*, 2017, **72**, 94-98.
135. R. J. Jiménez-Riobóo, N. Gordillo, A. de Andrés, A. Redondo-Cubero, M. Moratalla, M. A. Ramos and M. D. Ynsa, *Carbon*, 2023, **208**, 421-431.
136. H. Kimura, M. Sasaki, Y. Morimoto, T. Takeda, H. Kodama, A. Yoshikawa, M. Oyaidzu, K. Takahashi, K. Sakamoto, T. Imai and K. Okuno, *Journal of Nuclear Materials*, 2005, **337-339**, 614-618.
137. D. J. Cherniak, E. B. Watson, V. Meunier and N. Kharche, *Geochimica et Cosmochimica Acta*, 2018, **232**, 206-224.
138. J. A. Pittard, M. Y. Lavrentiev and N. A. Fox, *Diamond and Related Materials*, 2024, **149**, 111665.
139. M. Sasaki, Y. Morimoto, H. Kimura, K. Takahashi, K. Sakamoto, T. Imai and K. Okuno, *Journal of Nuclear Materials*, 2004, **329-333**, 899-903.
140. M. Bernard, A. Deneuville and P. Muret, *Diamond and Related Materials*, 2004, **13**, 282-286.
141. A. Deslandes, M. C. Guenette, C. S. Corr, I. Karatchevtseva, L. Thomsen, G. R. Lumpkin and D. P. Riley, *Nuclear Fusion*, 2014, **54**, 073003.